Modeling of heat transfer in structured ceramic materials

ETH
Eidgenössische Technische Hochschule Zürich
Swiss Federal Institute of Technology Zurich

Modeling of heat transfer in structured ceramic materials

Master's Thesis

Fabian Müller

April 21, 2020

Advisors: Prof. Dr. A. Steinfeld, Dr. F. Dähler

Department of Mechanical and Process Engineering, ETH Zürich

Tutor: Prof. Dr. S. Coros

Department of Computer Science, ETH Zürich

Abstract

Solar technologies for producing hydrocarbon fuels from solar energy have shown promising results in small-scale applications over the last decade. A thermochemical redox reaction using ceria as reduction material allows the splitting of H_2O and CO_2 and generating a mixture of CO and H_2, the precursors to liquid fuels. The shape of the ceria structure in the solar reactor cavity plays a critical role for the overall solar-to-fuel efficiency of the reactor. However, current ceria structures suffer from large temperature gradients and scale-up problems. While the design of these structures is based on simplified models and experience, sophisticated models are needed to analyze future structure designs.

During this thesis, a virtual simulation environment for analyzing the heat transfer in structured ceramic materials was developed. The simulation is based on the Monte Carlo radiative heat transfer method and allows to analyze the heating behavior of user-defined 3-D structures under conditions that are expected in a solar reactor cavity. The predicted heat distributions can be used to distinguish good from bad structure shapes, before the structures are physically manufactured. The simulation application is implemented in C++ and can be used on standard personal computers.

To illustrate the potential of the simulation environment, a novel ordered structure design is presented. Three basic structure shapes following this design scheme are analyzed and compared based on the heat distributions predicted by the simulation. These experiments have shown that the developed simulation environment can provide a basis for future ceria structure design processes.

Acknowledgements

I wish to express my sincere thanks to Dr. Fabian Dähler, my direct supervisor at the Professorship of Renewable Energy Carriers (PREC) of the department of Mechanical and Process Engineering, ETH Zurich, for the great support during the whole thesis.

I would like to thank Prof. Dr. Aldo Steinfeld, head of the Professorship of Renewable Energy Carriers (PREC) of the department of Mechanical and Process Engineering, ETH Zurich, for the opportunity to work in his research group during the last six months.

I would also like to thank my tutor Prof. Dr. Stelian Coros, head of the Computational Robotics Lab of the department of Computer Science at ETH Zurich, for the opportunity to write my Masters's thesis under his supervision.

Contents

Chapter 1

Introduction

1.1 Motivation

High expectation is placed on solar energy to reduce greenhouse gas emissions and mitigate climate change. The development of solar technologies over the past 30 years led to high efficiency increases and cost reductions [2]. While direct solar energy amounts to a small fraction of the total energy production today, it has the potential to become one of the major sources of energy supply worldwide until 2050 [2].
The solar energy that arrives at the Earth exeeds the energy consumption of humankind by a factor of about 10,000 [2]. Technologies such as photovoltaics (PV) and concentrating solar power (CSP) have proven to be able to convert solar energy into electricity in large-scale industrial production. Photovoltaic cells produce electricity directly, CSP plants produce high-temperature heat and use heat engines and generators to deliver electricity [2]. However, not all energy demand sectors can easily be electrified. Additionally, solar energy is variable and unpredictable up to some degree [12].
With the sun as a huge power source, the major challenge in the chain from solar energy production to consumption is therefore the intermediate energy carrier [18]. A highly promising field of research is the generation of hydrocarbon fuels, also known as solar fuels. While solar fuels can be used as an intermediate storage medium for electricity generation, their most valuable application is probably in the transport sector, especially in aviation due to their high volumetric and gravimetric energy density [10].

The three dominant technologies for producing solar fuels are *elctrochemical*, *photochemical/photobiological*, and *thermochemical* processing [2]. The latter uses solar heat, usually at high temperatures, combined with an endothermic thermochemical process [35]. A thermochemical redox reaction allows the splitting of H_2O and CO_2 and generating a mixture of CO and H_2, also known as syngas. A Fischer-Tropsch synthesis can further process syngas to liquid hydrocarbon fuels, such as diesel or kerosene [32].

In a solar chemical reactor, the reaction material plays a critical role. It has shown that oxides based on cerium dioxide (ceria) fulfill some of the desired properties, such as fast kinetics and chemical stability, even in long-term usage [14]. The geometrical structure of the ceria element is one of the key factors that determine the overall efficiency of the solar reactor. The ceria structure must be optimized for several conflicting goals: Generally, a high mass load is needed for maximum fuel output. During the endothermic reduction step, a structure allowing for uniform heating is desired. In the exothermic oxidation step a high specific surface area supports rapid reaction kinetics. Additionally, the structure should feature high mechanical stability under fast heating rates and high temperatures [19].
The design of current ceria structures is based on simplified models and experience. The analysis of reticulated porous ceramic (RPC) foam-type structures with variable pore sizes [14] and ordered structures [19] indicates that the main efficiency issue is the large temperature gradient across the structure that is observed during the endothermic reaction phase. Some parts of the structure do not even reach reaction temperature and become undesired heat sinks [14, 19].
Sophisticated models are needed to analyze and further improve current structure designs. The analysis of digital prototypes usually saves time and money compared to experiments with physical ones. Appropriate virtual simulation environments and methods are therefore of special interest. In this thesis a simulation environment based on the Monte Carlo radiative heat transfer method was developed [21]. It is implemented in C++ and allows to analyze the heat-up behavior and steady-state conditions of user-defined 3D structures.

While commercial tools such as COMSOL [8], open source tools such as openFOAM [38] and tools from other research groups [34, 6] are available, an in-house developed software has multiple advantages: It is tailored for the special needs of the research group and therefore minimize time and effort for researchers from this group to get familiar with the tool. Compared to commercial software, in an in-house solution all assumptions, the entire modeling and actual implementation are accessible and can be reviewed. Furthermore, it can be gradually improved and extended, whenever new research ideas come up in this group. To base a research project on non-commercial, external software can run into problems as such software tends to get outdated and lacks of support and maintenance unless a big community is using it.

1.2 Thesis outline

Chapter 2 discusses some relevant theory for this project. This includes the thermochemical redox-cycle in a solar reactor and covers problems with current ceria structure designs. Furthermore, automated design procedures in the field of topology optimization and the Monte Carlo ray tracing method are covered.
Chapter 3 describes the model used for the simulation application. It discusses the assumptions and simplifications used for approximating the true physical aspects of materials and heat transfer. The developed algorithms for a heat-up and a steady state simulation are explained.
Chapter 4 covers the actual software implementation. It discusses how the developed application was verified, presents some performance analysis and describes how the current implementation could be improved further.
Chapter 5 discusses design guidelines for ordered ceria structure. A novel structure design is presented. The potential of the developed simulation environment is demonstrated by the experimental analysis of three structure shapes.
Chapter 6 contains a conclusion of this thesis and discusses how the developed application could be used in concrete design optimization procedures.

Chapter 2

Theory

2.1 Two-step solar thermochemical redox-cycle

Among multiple pathways to generate fuels from sunlight, thermochemical processes that use concentrated solar energy seem very promising [32]. As solar thermal processes operate at high temperatures and make use of the entire solar spectrum, they have the potential for achieving high solar-to-fuel energy conversion efficiencies [32].
Thermochemical redox-reactions allow the splitting of H_2O and CO_2 to generate a mixture of CO and H_2, which is also known as syngas [32]. Most solar thermochemical reactors use a metal oxide as reactive intermediate and operate in a cyclic rhythm, while each cycle consists of a reduction and an oxidation step [32]. In the endothermic reduction step, the reaction material is heated through concentrated solar energy which induces a reduction of oxygen. The released oxygen leaves the solar reactor through gas outlets [15]. For the exothermic oxidation step, the high flux irradiation is stopped and H_2O and/or CO_2 enters the reactor through gas inlets [15].
The reduced metal oxide reacts with H_2O and/or CO_2 to produce H_2 from H_2O and/or CO from CO_2 [32]. This mixture of CO and H_2 (syngas) can be further processed to liquid hydrocarbon fuels, such as kerosene or diesel, e.g via Fischer-Tropsch synthesis [32]. For producing syngas, splitting of CO_2 and H_2O in separate cycles seems to be a promising approach, as the H_2 to CO ratio in syngas is then easier controllable in a further mixing step [26].

Among a wide range of metal oxides that has been studied for the usage in solar reactors, nonstoichiometric *cerium dioxide* (ceria, CeO_2) became the current state-of-the-art [7, 19]. It has shown that oxides based on ceria fulfill some of the desired properties, such as fast kinetics and chemical stability, even in long-term usage [1, 7, 14].
The two steps of the redox reaction cycle of pure ceria are described as follows:

1. High-temperature, endothermic reduction:

$$CeO_2 \rightarrow CeO_{2-\delta} + \frac{\delta}{2}O_2$$

2. Low-temperature, exothermic oxidation:

$$CeO_{2-\delta} + \delta H_2O \rightarrow CeO_2 + \delta H_2$$

$$CeO_{2-\delta} + \delta CO_2 \rightarrow CeO_2 + \delta CO$$

where the non-stoichiometry δ denotes the reduction extent [1]. The entire production chain from H_2O and CO_2 to solar fuels using nonstoichiometric ceria has been demonstrated. Not chemistry but system scale and design were identified as the major limiting components in the process [7]. The efficiency of ceria can even be improved by doping its fluorite structure with transition metals, which increases the amount of released oxygen for a fixed oxygen partial pressure and temperature [19, 32].
The next section describes how a two-step solar thermochemical redox cycle is realized in a solar reactor using ceria as reaction material.

2.2 Solar thermochemical reactor

Solar thermochemical reactors use concentrated solar radiation as energy source. The core of the reactor is a well-insulated cavity that has only a small aperture, through which the concentrated solar radiation enters. As the aperture is relatively small compared to the cavity volume, incoming solar radiation gets "trapped" in the cavity and undergoes multiple reflections with small probability of leaving the cavity through the aperture [30]. Therefore, the fraction of absorbed energy is significantly larger than the actual

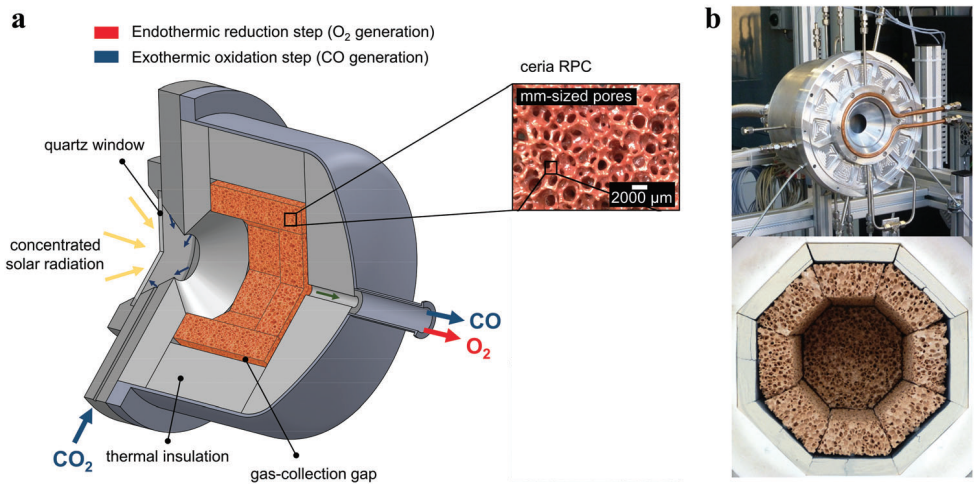

Figure 2.1: (a) Schematic of a solar thermochemical reactor. It consists of an insulated cavity with a small aperture for incoming concentrated solar irradiation. The aperture is sealed by a quartz window, allowing for operation under controlled pressures. The cavity contains a reticulated porous ceramic (RPC) structure made of ceria. Red arrow: Oxygen is released during the endothermic reduction step. Blue arrows: CO is produced from CO_2 during the exothermic oxidation step. (b) Photographs of the High Flux Solar Simulator (HFSS) of ETH Zurich showing the outer front and the interior containing an octagonal RPC structure. This figure is adapted from [26].

surface absorptance of the structure inside the cavity [30].

In order to give a concrete example of a solar thermochemical reactor, the High Flux Solar Simulator (HFSS) of ETH Zurich will be discussed next. While other solar reactors have different designs and characteristics, they share the main principles of this technology [30, 35]. A schematic of the HFSS is shown in Figure 2.1. The reactor volume is sealed by a quartz disk window, which allows to operate the reactor under controllable pressures. The cavity is filled with a reaction material, in this case an RPC structure which will be further described in a following section. An Al_2O_3-SiO_2 thermal insulation surrounds the cavity for minimizing energy loss by conduction through the reactor walls [26, 15].

The solar reactor is operated in cycles consisting of an endothermic reduction step and an exothermic oxidation step. Usually, the duration of each step is around 15 minutes [26].

In the reduction step, concentrated solar energy enters the cavity through the aperture and the ceria structure heats up. This induces a release of oxygen which leaves the reactor through the gas outlet. Temperatures during the reduction step are typically around 1773 K and total pressure is fixed at 10 mbar using a vacuum pump [26]. Much higher average temperatures should be avoided, as ceria sublimation could be observed at temperatures around 2250 K [15].
For the subsequent exothermic oxidation step, the solar irradiation is stopped and CO_2 and/or H_2O enters the reactor through the gas inlets. Thus, the reactor is re-pressurized to a total pressure of 1 bar. The partially reduced ceria is then re-oxidized at temperatures below 1273 K [26]. The produced H_2 and/or CO leaves the reactor through the gas outlets and when the ceria structure is largely re-oxidized, the cycle can start over again.
In lab-scale experiments with 4 kW solar radiative power input a solar-to-fuel energy efficiency of 5.25% could be achieved [26].

In most solar reactor designs, such as in the HFSS, the reaction material (ceria) is directly exposed to the high-flux irradiation. The analysis of a scaled-up model (50 kW solar reactor) showed that re-radiation that leaves the cavity through the aperture is expected to be the dominant source of heat loss [39]. The expected energy balance for a reduction step of around 12 minutes can be seen in Figure 2.2.

Re-radiation losses account for 31% of the total energy input on average and 45% at the peak. The heating of the bulk materials, such as the Al_2O_3-SiO_2 insulation, consumed 21% of the total energy input on average. The heating of the RPC structure consumed 31% and the endothermic reaction accounts for 5.6% of the total energy input. Another significant heat loss is the absorption and reflection of incoming radiation at the quartz window, where 7.1% of the incoming energy is lost. The water cooling of the front accounts for 2.7% of the energy consumption. The heat loss by conduction through the reactor walls plays a minor role with less than 0.3% of the total energy input [39].

A previous reactor design ([15]) was less insulated and therefore the heat loss by conduction through the cavity walls was significant and accounted

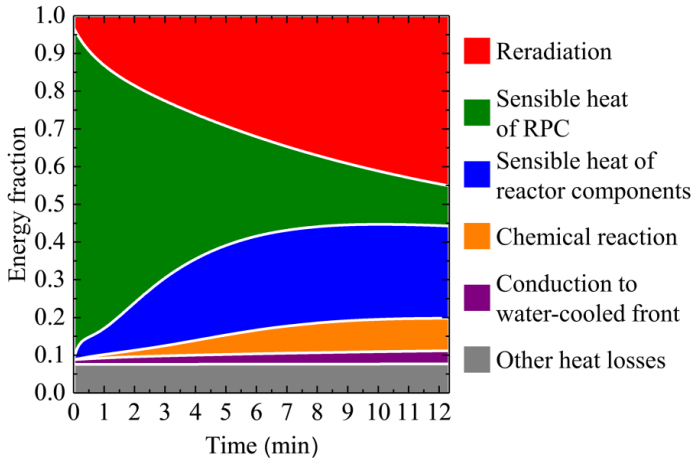

Figure 2.2: Modeled energy fractions versus time during the reduction step in a 50 kW solar reactor. Other heat losses include: convection and radiation at the outer reactor surfaces, reflection of incoming solar radiation inside the reactor cavity, absorption and reflection at the quartz window. This figure is copied from [39].

for 17%. However, less energy was lost for heating up the insulation. The heating of the ceria material and reactor components together accounted for 31% in the previous reactor design [15]. In the newer design, they account for 54% together. It must be noted that the re-radiation loss differs a lot (48% in the previous, 31% in the newer design) and the two reactor designs also differ in dimension and mass loads, therefore such relative values can easily lead to wrong interpretations. However, it can be seen that a thicker insulation decreases the heat loss by conduction and convection at the reactor wall, but consumes more energy to be heated. Insulation materials with lower specific heat capacity would lower this energy loss [39].

It is notable that heat loss by conduction through the reactor walls plays a minor role in large reactors compared to small reactors, due to the smaller surface-to-volume ratio [26]. This could be experimentally verified [26, 39]. However, heat loss through re-radiation remains problematic in scaled-up models. In order to minimize heat loss through re-radiation, optimized reaction material layouts are needed. The next section describes the current challenges in the design of such ceria structures.

2.3 Problems with current ceria structures

The particular shape of the ceria structure is critical for the performance of a solar reactor. [19] and [13] identified multiple conflicting topology goals for the design of optimized ceria structures: To achieve maximal syngas output from the redox-cycles, the mass of redox material should be maximized for a given volume of the solar reactor cavity. The endothermic reduction step depends on the heat distribution across the structure, which requires appropriate optical thickness that allows for a uniform heating behavior. As the exothermic oxidation step is mainly surface/mass controlled, a high specific surface area is desired.
Filling a given reactor volume with non-transparent mass inevitably decreases the amuont of radiation that reaches the rear part of the reaction structure close to the cavity boundary. This indicates the conflict of the previous mentioned goals [19].
Furthermore, it is important that the structure features high mechanical stability over a large number of cycles. It must operate under fast heating rates and is exposed to high temperatures. CeO_2 starts to release oxygen at a temperature around 1173 K [7] and is usually heated up to temperatures exceeding 1773 K in current reactor designs [15, 29].

The shape of the reactor cavity, the distribution of the incident concentrated solar radiation and material properties of the reactor are further boundary constraints which must be considered when designing an optimized ceria structure. Experiments have shown that depending on the reactor design, a uniform distribution of the incident solar radiation on the ceria structure cannot be guaranteed [15]. This leads to hotspots with undesired temperatures of up to 2250 K, which induces CeO_2 sublimation and therefore a deformation of the original structure shape [15].

2.3.1 Reticulated Porous Ceramic (RPC)

The current standard for ceria structures in solar reactors are so called reticulated porous ceramic (RPC) foams [19]. The foam-like structure is not ordered and usually features dual-scale porosity. The mm-sized pores largely

define radiation penetration depth and contribute to better radiative heat transfer. The micron-sized pores on the RPC struts support faster oxidation kinetics [29].
As the porosity is uniform in RPC structures, incident radiation undergoes attenuation following Bouguer's law, meaning that the intensity of solar radiation decreases exponentially with the penetration depth [1, 13, 19, 23]. This leads to large temperature gradients during the heat-up phase with hotspots on the front side and undesired low temperatures on the rear side close to the cavity boundary [15, 19, 39]. To overcome this problem, RPC structures with different porosity and pore diameter have been tested in lab-scale and designs with variable porosity and pore sizes were suggested [1, 39].
The current standard method to create RPC structures is the *replication method* [33]. It uses polymer foam templates which are then coated with a ceria-based slurry and sintered at a temperature around 1873 K [19, 29]. During sintering the polymer template is burned and a solid RPC structure remains.
The fabrication of RPC structures with high porosity and large pore sizes showed various challenges. The larger the pores, the more fragile the structure is [19]. Pore sizes which showed promising results in lab-scale would have to be drastically increased for scaled-up applications and it is unclear whether large-scale RPC structures will ever fulfill the stability and porosity requirements at the same time [19, 39].

2.3.2 Ordered ceria structures

As discussed in the previous section, RPC structures mostly suffer from scale-up problems, as it is difficult to fabricate a structure which features appropriate optical thickness as well as high mechanical stability. [19] presented a structure design that follows a hierarchical ordering. Elementary cell blocks of different sizes were used to enabled a non-uniform porosity in the composed structure. Among different cell geometries, a cube skeleton consisting of ceria struts for all edges and some diagonals was chosen based on experimental results [19]. This basic cube cell geometry can be seen in Figure 2.3 (a). The different-sized cell blocks were arranged so that large cells (with low optical thickness) were placed at the front side and small

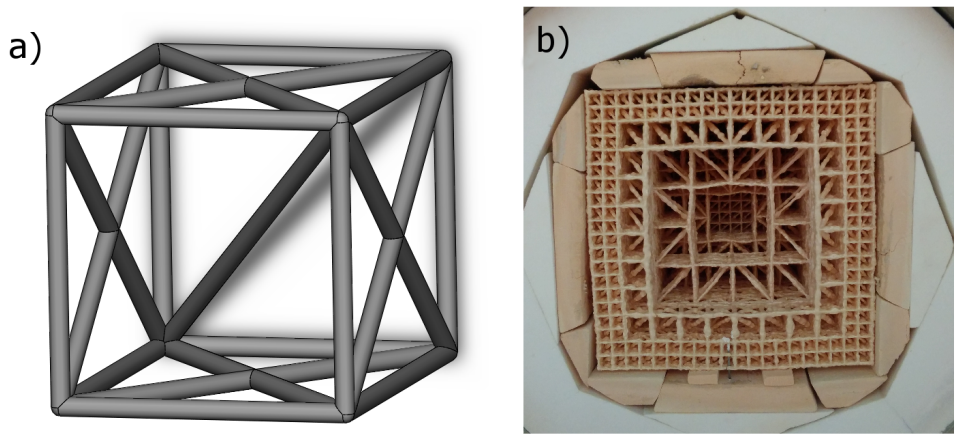

Figure 2.3: Design of an ordered structure made of ceria. (a) Base cell geometry. (b) Photograph of the entire structure composition, consisting of multiple base cell geometries of different sizes. This figure is adapted from [19].

cells (with high optical thickness) were placed at the rear side of the structure. A picture of the resulting composed structure can be seen in Figure 2.3 (b).

This composition results in a porosity which decreases from the front to the rear part and therefore supports volumetric absorption. A smaller temperature gradient across the structure was expected compared to an RPC structure of similar mass [19]. However, measurements from the experiments in a 4 kW solar reactor showed a significant lower temperature in the rear side for the ordered structure compared to the RPC structure. This indicates a higher temperature gradient for the ordered structure, in contrast to the prior expectations [19]. As most of the mass in this composition is located at the rear side, the overall performance (in terms of oxygen release) was calculated to be around 10% worse than in the RPC structure. The poor heating of the rear part was attributed to blocking of radiation by ceria struts in the front [19].

Additionally the designed ordered structure showed strongly damaged parts after 26 cycles, as can be seen in Figure 2.4. The inner part collapsed to a large amount, yielding a significantly different topology compared to the original design.

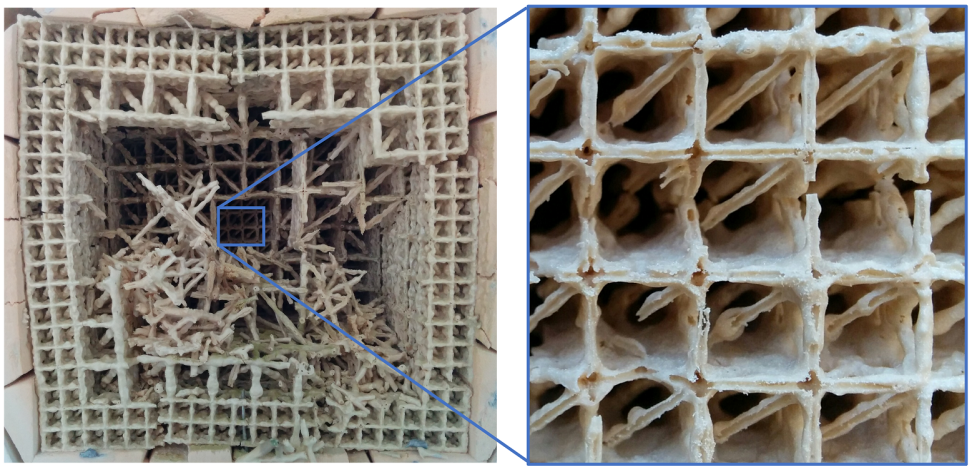

Figure 2.4: Photograph of the damaged ordered structure after 26 cycles. Fast heating rates and high temperatures led to thermal stress and sublimation, which caused a partial collapse of the structure. This figure is copied from [19].

The reasons for this deformation seem to be sublimation of ceria and thermal stress induced by the fast heating rates [19]. Sublimation of ceria at hotspots was also observed in pervious studies [15]. It seems that RPC structures can handle small expansion and contraction from thermal stress and deformation from sublimation pretty well due to its foam-type structure. For further structure design, these material properties should not be underestimated when predicting mechanical stability.

2.3.3 Structure manufacturing

In the chain of production of ceria structures, the limiting factor with respect to precision is the physical manufacturing. So far, ceria structures have usually been produced by coating a polymer structure with a ceria-based slurry, followed by a sintering process. The precision of this process is limited to a range above a tenth of a millimeter [19]. The ordered structure in Figure 2.3 (b) was fabricated with a polymer diameter of 0.4 mm. After several layers of coating, the strut thickness (that should be uniform) largely varies, as can be seen in Figure 2.3 (b).

A promising approach is the direct 3D-printing of ceria structures, which

is technically feasible already [27]. However, it is not yet commercially established, due to the limited field of application [19]. The mimimal layer thickness that can be 3D-printed nowadays is around 0.35 mm, the minimal wall thickness (based on a nozzle of size 0.41 mm) is around 0.37 mm after sintering [11].

2.4 Topology optimization

As previously mentioned, current ceria structures are modeled based on simplified models and experience. To reach a design process beyond that, models which allow for mathematical optimization of the ceria structure before physical manufacturing are needed.

One rapidly growing field in heat transfer research is called *topology optimization* (TO). TO is viewed as a highly promising automated design procedure, in which optimized structures for various applications are generated [25]. Following a set of equations from physics theory and user-defined boundary conditions and optimization goal, an optimized material layout in a predefined volume can be found.

During the last three decades, computational design procedures made strong progress due to the increased computational power and improvements in numerical optimization methods [25]. Common modern solvers use a variant of the Finite Element Method (FEM), where the design space is discretized at a defined granularity. By iteratively choosing whether a finite element should be "filled" with material or left as "void" space, a three dimensional structure is generated [25]. Nowadays, the majority of TO solvers consider only conduction and convection but not radiation [25, 9, 36]. However, as we have seen in a previous section, heat transfer in ceria structures is mainly driven by radiation.

As the shape of the structure changes continuously in an iterative optimization method, the temperature distribution must be recalculated in each iteration. Especially view factor computation, which is crucial for estimating radiative heat exchange, is non-trivial and very expensive to perform exactly [25]. However, temperature distributions can be approximated with numerical methods, such as the Monte Carlo Ray Tracing (MCRT) method which

is described in the next section. The tool developed in this thesis could be used as a component in a topology optimization method. Even though it goes beyond the scope of this thesis, TO has great potential for designing optimized reaction material layouts and will be picked-up in the outlook section of this report again.

2.5 Monte Carlo simulations for radiation heat transfer

[19] analysed a basic cube geometry in an exemplary CFD simulation and showed that conductive and convective heat transport within the ceria structure is negligible compared to the radiative transport. Under reasonable temperature and gas velocity assumptions during operation of a solar reactor, the fraction of conductive and convective heat transport together represented less than 2% of the incoming radiative flux [19]. The radiative heat transfer in the reactor cavity is therefore of special interest.
For analyzing the heating behavior of a non-trivial structure, the mathematical equations which describe radiative heat transfer are complex and difficult to solve with reasonable accuracy. Material and surface properties further increase the complexity of calculations in deterministic methods [21].
Among several different computational methods with which radiative heat transfer problems can be analyzed, Monte Carlo methods are very popular. A Monte Carlo method is a numerical technique that allows the simulation of physics-driven models based on statistical characteristics of the actual physical processes [21].

To analyze radiative transfer processes, the radiative energy is discretized into rays or bundles / packets of energy that leave a specific surface element. A large number of rays, each carrying a small amount of energy, are simulated, similar to the beahvior of photons [21]. Each ray is traced from the source surface until it strikes a different surface element in the simulation scene. Depending on the physical properties of the struck surface, a fraction of energy is absorbed at the hit point while the remaining energy is reflected, simulated by another ray. By the end of the simulation of all rays, one can then analyze the energy distribution in the system.

It is crucial that the distributions of the ray origins and directions follow the underlying true distributions according to the laws of radiation [21]. The ray origins and directions must therefore be sampled at random from distributions that approximate radiative behavior well. Due to the statistical nature, the larger the number of rays considered, the more exact the heat distribution of the Monte Carlo simulation is [21].
While the idea behind Monte Carlo methods is usually relatively simple and intuitive, they often require a lot of computation. However, if each event (e.g tracing of a single ray) can be computed independently of other events, a high degree of parallelization is possible. The following sections about the used simulation model and the actual implementation discuss how the Monte Carlo ray tracing method is applied to the heat transfer problem covered in this thesis.

Chapter 3

Model description

This chapter describes the model that was used to simulate the heating behavior of a ceria structure in a solar reactor. The main target of the simulation is to distinguish good from bad structure shapes before they are physically manufactured, which enables an optimized design process. As discussed before, the major objectives for the structure are high mass, large specific surface are and uniform heating across the structure [19, 13]. The developed model and simulation are both based on assumptions and simplifications that differ from reality. Nevertheless, it is expected that it is still possible to identify positive and negative design properties for real applications. Two different simulations were implemented: one that calculates a heat distribution at steady state and one that simulates the heat-up process. The heat-up process will eventually reach steady state as well, the direct steady-state simulation is much faster, however. We have seen earlier that the reactor is not heated until a complete steady state is achieved during the reduction step. Therefore the heat-up simulation seems to yield more valuable information for our structure design.

3.1 Geometries and materials

In the developed simulation, the actual physical properties of the reactor components are approximated. This section describes assumptions and simplifications that are relevant for radiation heat transfer.

3.1.1 Triangulated surface mesh

Each geometry that is used in the simulation is represented as a triangulated surface mesh, meaning the surface of an object is approximated by a set of connected, two-dimensional triangles. A triangulated surface mesh only consists of vertices (points in 3D space) and triangles (sometimes called faces) which connect the vertices. Surface normals are usually derived from the triangle normals.
The flat triangle is a constant curvature approximation for the curved surface at a given location. Increasing the amount of triangles in a surface mesh allows for a better approximation of the actual shape, as the triangles get smaller and therefore the triangle normals get closer to the actual surface normals.

As discussed earlier, the limiting factor for precision in the production of ceria structures is the physical manufacturing part. Assuming that ceria structures can be printed with a precision of 0.35 mm, the mesh surface should have at least this precision as well. The vertices of the surface mesh are positioned with floating point precision (32 bit, also known as *single precision*), which is again much preciser than the physical manufacturing. Assuming dimension units in meter are used, a precision below 1 micrometer can be achieved with floating points.

3.1.2 Volume representation

While a surface representation (such as a triangulation) of an object is efficient for a Monte Carlo ray tracing algorithm, it lacks of information about the volume that is associated to a discrete surface area.
The developed steady-state simulation is based on the surface areas but not on the associated volume of discrete elements, as we will see soon. For that, the triangulation of the surface mesh is a sufficient representation of the object to analyze. On the other hand, the developed heat-up simulation depends on the volume that is associated with a surface element. For that, a constant thickness is associated to each triangle of the surface. While this approach is simple, it induces an error in curvy areas of the surface. Neighboring volume elements would actually overlap in convex parts and

therefore overestimate the actual volume behind this part of the surface area. In concave regions, the actual volume associated to a surface patch would be underestimated, as there will be gaps between neighboring volume elements. Additionally, if one part of the structure is very thin (less than two times the triangle thickness), the volume elements associated to the opposite walls would overlap in the middle of the structure.

As conduction is not considered in the used model, a volume representation of the entire object seems to be an unneeded overhead. However, an improvement of the actual model would be to calculate the volume associated to a triangle element on the surface based on the surface curvature at this location. This would be one pre-processing step, if the structure is assumed not to change its shape due to temperature changes during the simulation. Options for this calculation have been discussed but it was not implemented yet due to time limitations.

3.1.3 Material properties

For all materials in the simulation, the surfaces are assumed to be diffuse, gray and opaque. The gas mixture in the reactor is assumed to be a non-participating media.

Some material properties such as reflectivity, absorptivity / emissivity and specific heat capacity are temperature dependent. In a first phase of the model development, these properties are set to a constant value for the steady-state and heat-up simulation.
In a second phase of the heat-up model development, these material properties should change with the corresponding temperature. This is not fully implemented yet, and therefore average values for the expected temperature range must be chosen by the user.

3.1.4 Simulation environment

The simulation environment consists of a light source and a variable amount of solid objects. The light source and all solid objects are represented as triangulated meshes which are specified by the user input. For example, as-

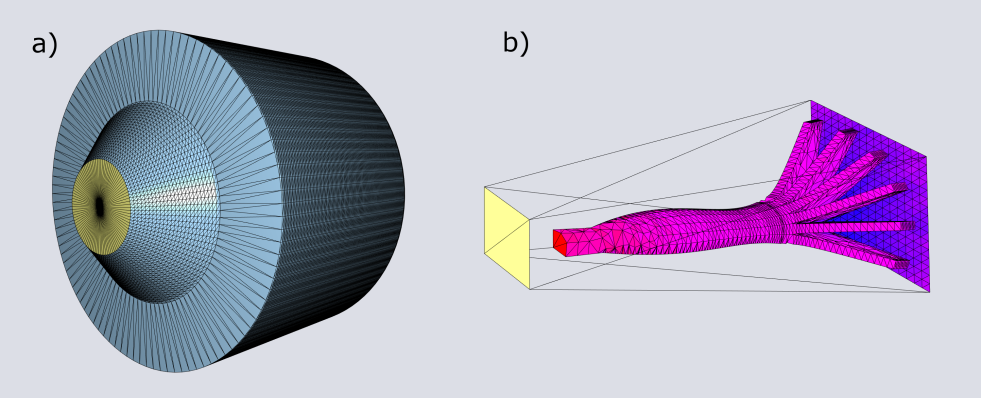

Figure 3.1: Illustration of two example simulation environments. (a) 3-D model of an entire solar reactor cavity. The yellow area indicates the aperture (light source in the simulation), the light-blue area indicates the cavity boundary. (b) 3-D model of a segment of a reactor cavity during the heat-up simulation. The yellow area indicates the energy source in the simulation, which is towards the cavity center. The red-purple geometry is the ceria structure, the blue-violet area is the cavity boundary. Transparent faces are mirrors in the simulation.

suming one would like to simulate the heating behavior in a solar reactor. The light source would be a (flat) disk in the shape of the aperture, one (or several) solid objects would represent the cavity boundary and one (or several) solid objects would represent the ceria structure in the interior. Two example simulation environments can be seen in Figure 3.1. Beside simulating the heating behaviour of an entire solar reactor cavity, it might also be interesting to simulate only a specific segment in it. Using mirroring faces as segment boundaries, multiple neighboring segments can be simulated that way.

The user is responsible for providing meshes that do not contain holes and are correctly oriented. Meshes do not have to be closed, meaning not actual 3D volumes must be enclosed by a mesh. This means, for the light source, a flat disk and for the solids that represent the cavity boundary, the inner walls are sufficient.

3.2 Heat-up simulation

To simulate the radiative heat transfer, a Monte Carlo ray tracing method was implemented. The ray tracing is the fundament of both the steady state and heat-up simulation. However, the actual algorithms differ in the two scenarios. During the development, the steady state simulation was implemented first, as it is easier to implement. However, for this report, the heat-up simulation is discussed first, as it follows a rather intuitive idea and seems therefore to be suited for being discussed foremost.

3.2.1 Basic algorithm

The simulation runs over a fixed number of rounds, each round has a predefined round time. Each solid is initialized with a starting temperature, the light source is assigned a constant radiant power.
At the beginning of a round, for all solid triangles the radiant power must be emitted. This calculation follows the Stefan-Boltzmann law

$$P_{i,j} = A_i \varepsilon_{i,j} \sigma T_{i,j}^4 \tag{3.1}$$

where $P_{j,i}$ denotes the radiant power, A_i the area, $\varepsilon_{i,j}$ the emissivity, σ the Stefan Boltzmann constant and $T_{i,j}$ the temperature of triangle i in round j. Note that in this formula the emissivity is temperature dependent, even though it is not yet fully implemented in the current version of our simulation.

For light source triangles, the power per triangle is proportional to the triangle area. Together with the round time, the amount of energy that must be emitted from each triangle during the current round is found:

$$Q_{i,j}^E = P_{i,j} * t_j \tag{3.2}$$

where $Q_{i,j}^E$ denotes the emitted energy, $P_{i,j}$ the radiant power of triangle i and t_j the round time in round j.

The heat-up simulation then follows the "classic" Monte Carlo ray tracing scheme as it was introduced in the theory section. A predefined *average ray energy* determines the amount of rays that are emitted from a triangle in this round. The actual energy $Q^E_{i,j}$ that must be emitted from triangle i is then divided among the rays that will start form this triangle. This ensures that the total amount of energy in the system follows the law of conservation of energy.

Each ray starts at a position that is sampled uniformly at random from the triangle. The direction of the ray is determined by the assumption of diffuse surface radiation, meaning the ray directions are sampled cosine-weighted from the unit hemisphere around the sampled starting position [21]. For the light source, the user has the possibility to limit the angle of emissive radiant flux, which is desired to simulate concentrated solar irradiation in a solar reactor. For rays from light source triangles, the direction sampling will then not be from the entire hemisphere, but only from a restricted angle around the triangle normal.

Each ray is then traced from the sampled starting point along the sampled direction. The first intersection of the ray with a solid object is computed, which denotes the *hit point* of this ray. Based on the reflectivity/absorptivity of the solid object, the amount of energy that is absorbed at the triangle is calculated and deposited (added to the triangle's absorbed energy of this round). The remaining ray energy is reflected. A new direction is sampled according to the distribution for diffuse reflection. A new ray is then traced from the hit point along the new direction, determining the next intersection point. This procedure repeats until the ray leaves the system through the light source (meaning a ray hits the light source geometry and is stopped) or the carrying energy drops below a certain threshold. If the ray energy is below the threshold, the reflection / absorption at a triangle follows an "all or nothing" principle: The remaining energy is either fully absorbed and the ray is stopped, or it is fully reflected. The probability for n more reflections (without absorption) after the ray energy dropped below the threshold is therefore

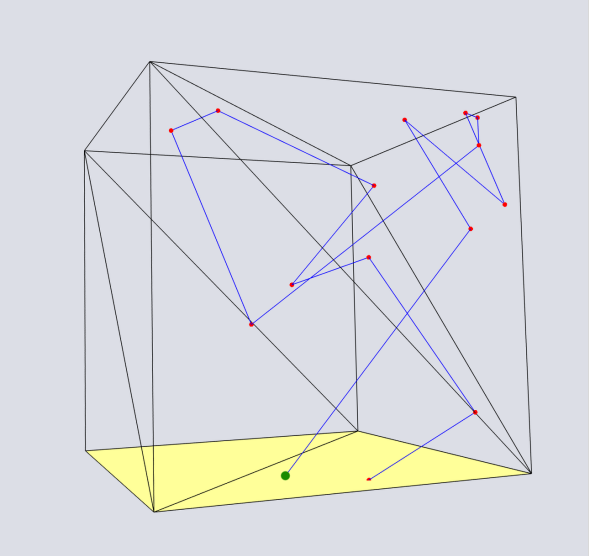

Figure 3.2: An example ray path in a simple cube cavity with diffuse surfaces. The yellow area indicates the light source. The first sampling point (start) is indicated by a green dot, red dots indicate intersections, where the ray was absorbed and re-emitted or reflected.

$$Pr[Z = n] = \rho^n \tag{3.3}$$

where Z is a random variable that denotes the number of reflections below the threshold and ρ denotes the reflectiviy $\in [0, 1)$. This probability function is exponentially decreasing, meaning that rays that are not stopped for a long period are very unlikely. An exemplary ray path for a ray that finally left the simulation environment through the aperture (light source) can be seen in Figure 3.2.

When all rays from all triangles have been fully traced until they were stopped, the radiative heat transfer for this round is completed. At each triangle, the net energy exchange (the difference between the emitted and absorbed energy) for this round is calculated:

$$Q^A_{i,j} = \sum_r q_{r,i,j} \tag{3.4}$$

$$Q^{net}_{i,j} = Q^A_{i,j} - Q^E_{i,j} \tag{3.5}$$

where $Q^A_{i,j}$ is the total absorbed energy and $q_{r,i,j}$ denotes the amount of energy that was deposited by ray r at triangle i in round j. $Q^{net}_{i,j}$ denotes the net energy exchange at triangle i in round j. From that, an increase or decrease of the triangle's temperature is derived:

$$\Delta T_{i,j} = Q^{net}_{i,j} / c_{i,j} \tag{3.6}$$

$$T_{i,j+1} = T_{i,j} + \Delta T_{i,j} \tag{3.7}$$

where $c_{i,j}$ denotes the heat capacity of triangle i in round j. $\Delta T_{i,j}$ denotes the temperature difference of triangle i from round j to round $j+1$ and $T_{i,j+1}$ the temperature in round $j+1$ accordingly. Using these updated triangle's temperatures, the next simulation round starts.

As we have seen, the described algorithm assumes a constant temperature across the entire area of a triangle. This is another approximation which can be improved with smaller triangle sizes.

3.2.2 Heat sinks

As discussed earlier, in current solar reactor designs the major sources of heat loss are the re-radiation through the aperture and the heating of the reactor components. Re-radiation, the heating of the ceria material and the remaining reactor components together accounts for around 85% of the energy consumption during the reduction step [39]. With the previously described simulation algorithm, these three heat sinks can already be approximated. The heat losses by conduction and chemical reaction are currently under development at the time of this report. They are not fully tested yet and therefore not used in the experiments, their current state of implementation is still described here.

Conduction through cavity boundary

As we have seen, with current insulation materials (such as Al_2O_3-SiO_2) it seems to be a trade-of between having less conductive heat loss with a thick insulation layer and having less bulk material to heat up with a thin insulation layer. Current reactor designs use rather thick insulation layers, which

leads to an almost perfect insulation.
Nevertheless, a heat sink for the cavity boundary was implemented. It accounts for conduction through the insulation layer and calculates the convective heat loss at the outer shell of the reactor. The implementation does not account for the metal reactor shell due to its very high thermal conductivity. A constant temperature gradient across the insulation layer and natural convection outside the reactor are assumed. For a cylindrical shell this assumption is reasonable as long as the insulation thickness is small compared to the cylinder radius. For one triangle, the conductive heat flux density per unit area q_{cd} (in $[\frac{W}{m^2}]$) can be found as follows:

$$q_{cd} = \alpha(T_I - T_O) = \frac{k}{L}(T_I - T_O) \tag{3.8}$$

where k denotes the conductivity of the insulation material, L the thickness of the insulation layer, T_I and T_O the temperatures at the inner and outer wall of the insulation layer. The convective heat flux per unit area q_{cv} (in $[\frac{W}{m^2}]$) at the outer reactor wall is

$$q_{cv} = h(T_O - T_A) \tag{3.9}$$

where h is the convective heat transfer coefficient and T_A is the ambient temperature. We known that the energy lost by conduction can only leave the outer reactor wall by convection. Therefore

$$q_{cd} = q_{cv} \tag{3.10}$$

$$\implies \alpha(T_I - T_O) = h(T_O - T_A) \tag{3.11}$$

must hold. Solving this for T_O yields

$$T_O = \frac{\alpha T_I + hT_A}{h + \alpha} \tag{3.12}$$

Due to the constant temperatrue gradient, the average (mean) temperature T_M of the insulation material is

$$T_M = \frac{T_I + T_O}{2} \tag{3.13}$$

When we plug in the formula for T_O and solve it for T_I we get

$$T_I = \frac{2(h + \alpha)T_M - hT_A}{2\alpha + h} \tag{3.14}$$

A fixed ambient temperature (e.g 273 K) is assumed. A common value for h is 15 $\frac{W}{m^2K}$ for such simulations [39]. The conductivity k depends on the material (and temperature).
Each segment of the cavity boundary (represented as a triangle) has an assigned mean temperature $T_{M,j}$ at the start of round j. Based on that, the inner and outer wall temperatures for this segment $T_{I,j}$ and $T_{O,j}$ can be found as showed previously. Using $T_{I,j}$, the radiative power for this segment at the inner wall can be found using the Stefan Boltzmann law (Eq. 3.1). Similarly, using $T_{O,j}$, the energy loss by convection at the outer wall can be found.

After each simulation round, the mean temperature $T_{M,j+1}$ of a discrete insulation element (triangle) for round $j+1$ is found based on the emitted and absorbed energy inside the cavity and loss by convection at the outside (using Eq. 3.6 and 3.7). The idea for this implementation of conduction heat losses is from [11].

Chemical reaction heat sinks
In each round, some energy is lost due to the chemical reaction in the ceria structure during the reduction step. As the used discretization for the ceria structure is a set of triangles with associated mass, the energy loss due to the chemical redaction must be calculated for each triangle. [4] analyzed how the oxygen release in ceria changes with temperature and pressure. Based on that, the energy loss due to the chemical reaction can be implemented as a function of temperature and ceria mass for a given triangle, assuming a constant pressure. This energy loss then contributes to the net energy of a triangle for the current round, together with the absorbed and emitted energy from the radiation simulation.

3.2.3 Adaptive round time

While radiation heat transfer is actually a continuous process, for the simulation some time discretization must be defined in order to get discrete amounts of energy that can be transferred from one point to another. Over this time period, the triangle is assumed to radiate at a constant temperature. The larger the time period, the larger the induced error, as if the net heat flux is not zero, then the temperature should change and so should the

radiative power (assuming no incident radiation).
Given the emissive power of a triangle, the round time defines how much energy is emitted from this triangle during the current round. The absorbed energy in a round depends on how many rays hit that triangle, which is stochastically determined in the ray sampling process and over- or underestimates the true value, due to the limited number of rays that are used. A simulated triangle's temperature therefore oscillates around the true value over the rounds, and the amplitude of the oscillation depends on the temperature and round time .

The first implementation used the same fixed round time for all rounds. This algorithm design has the following issue: A round time that seems reasonable for low temperatures might not be appropriate for high temperatures. If the round time is too high, a triangle can emit so much energy during this round that its temperature would potentially fall below 0 K, if not enough energy is received by absorption. The temperatures then oscillate so heavy that the entire system starts to diverge. Using only very conservative, low round times would lead to a very slow heat up progress for lower temperatures and therefore highly increase the number of heat-up rounds and computation time needed.

To overcome this issue, an *adaptive round time* was implemented. The idea is, that the user can define a maximal energy loss (relative, e.g 20%) that is allowed for any triangle in a round. Before a round starts, the maximal allowed round time is then computed for every triangle, using its associated radiative power and heat capacity:

$$t_{i,j}^{max} = T_{i,j} L c_{i,j} / P_{i,j} \tag{3.15}$$

where $t_{i,j}^{max}$ is the maximal allowed round time for triangle i in round j and L is the maximal energy loss that is allowed for any triangle during one round. The other symbols are defined as above. The reference temperature for $E = 0J$ would be at $T = 0K$. The minimum of these values $t_{i,j}^{max}$ then defines the current round time t_j^{round}:

$$t_j^{round} = \min_i t_{i,j}^{max} \tag{3.16}$$

In this way it is ensured that the amount of emitted energy is limited for every triangle and heavy temperature oscillations and temperatures below 0 K can be avoided. A best possible round time for the given constraints is found therefore. However, it must be noted that the round time can get very small, when the scene objects have small triangle areas, as the heat capacity is small as well in that case. Additionally, the round time strongly decreases with increasing temperature. This solution could therefore be improved in further development.

3.2.4 Energy saturation problem

Another interesting property that has to be taken into account is the impact of the limited amount of rays in the simulation. It is obvious that a simulation using a Monte Carlo ray tracing scheme gets more accurate, the more rays are used. In the described algorithm this means, the less the average ray energy is, the more rays will be used in the simulation. Initially it was expected that the simulation would heat up a system to its steady-state and then the temperature values would oscillate around the *true* steady-state values. The number of rays would determine the accuracy of the simulation and therefore define the amplitude of the oscillation.
During some verification tests, it was observed that the true steady-state values are not reached, however. The simulation had converged in the sense that in each round, the amount of energy that enters through the light source equals the amount of energy that leaves through the light source (assuming no other heat losses). But the observed temperature values were too low, clearly also the total energy that was absorbed in the system since the start of the simulation was too low.

What initially looked like an implementation bug is rather an approximation error from the model and can be explained as follows: Assuming two identical objects A and B start with the same, uniformly distributed temperature. Both surfaces are exposed to the same amount of radiative flux. Assuming

both surfaces absorb the same amount incoming radiation, but surface A absorbs it uniformly, while surface B does not (in our case: some triangles absorb more energy than others). Object A now has a homogeneous temperature distribution, while object B now has an inhomogeneous temperature distribution. But the radiative power of object B with the inhomogeneous temperature distribution is now larger than the radiative power of object A. This follows from the fact that the temperature increase of a triangle is linear with the absorbed energy, the radiative power however follows Stefan Boltzmann law which says $P \propto T^4$, with P indicating the radiative power and T the temperature.

Let's consider a simple example with a system that only contains two triangles X and Y that have an initial temperature of $T_X = T_Y = 10\ K$. Assuming both triangles have equal size and a heat capacity of 1 J/K, and the energy that enters the system over a given time period is 10 J. In system A, the incoming energy is distributed equally ($T_X = 15, T_Y = 15$), while in system B it is not ($T_X = 10, T_Y = 20$). The sums of the radiative powers (in [W]) yields $(15^4 + 15^4) * const = 101250 * const < (10^4 + 20^4) * const = 170000 * const$.

A proof sketch for this behavior follows below, let us analyze first what this means for the simulation. In steady state, the radiative power from the light source is equal to the re-radiative power of the objects, so that the net radiation of the system vanishes (the energy that enters through the light source equals the energy that leaves the system through the light source).
As the temperature distribution at steady state is always inhomogeneous (oscillating temperatures due to the limited amount of rays), the system is already "saturated" with energy before it could actually absorb the amount of energy needed, so that all triangles could reach the true temperature. This explains the observations described in the beginning of this section. A system with a homogeneous temperature gradient would re-radiate less, meaning more energy can be absorbed until it reaches a steady state re-radiation. To overcome this problem, a larger amount of rays with lower average ray energy is needed. This obviously increases computation time. However, a high accuracy of the temperature distribution is maybe not required throughout the entire simulation. In case some "checkpoints" are defined in time at

which one would like to evaluate the system, a high amount of rays could be used only during a few rounds before the checkpoints, and much less rays during all the other rounds. Compared to increase the amount of rays for the entire simulation, this speeds up the simulation but still yields good approximations for the evaluation at the checkpoints.
Two Figures (Fig. A.1 and Fig. A.2) that show the heat-up simulation behavior as described in this section are included in the Appendix A.1.

Proof sketch
A proof sketch for the described relation would include the following:

Given a constant s. For a function f,

$$f(x_1, x_2, ..., x_n) = x_1^4 + x_2^4 + ... + x_n^4$$

with constrained input space so that

$$x_1 + x_2 + ... + x_n = s$$

the minima is found at the location where $x_1 = x_2 = ... = x_n$.

Assuming there would be a minimum at $\boldsymbol{x}^*$ with at least two variables $x_i^* \neq x_j^*$. Then, a different solution $\hat{\boldsymbol{x}}^*$ where $\hat{x}_i^* = \hat{x}_j^* = (x_j^* + x_j^*)/2$ would yield $f(\hat{\boldsymbol{x}}^*) < f(\boldsymbol{x}^*)$. This can be geometrically shown as for two variables the constraint $x_i + x_j = const$ is a straight line in two dimensional space between $(x_i, 0)$ and $(0, x_j)$, and the function $g(x_1, x_2) = x_1^4 + x_2^4 + const$ has axis-symmetric, convex contour lines (nearly circular) around the origin. The intersection of the constraint with the lowest contour line is therefore at the point where $x_1 = x_2$. The fact $f(\hat{\boldsymbol{x}}^*) < f(\boldsymbol{x}^*)$ is a contradiction to the assumption that the inhomogeneous $\boldsymbol{x}^*$ is a minimum.

3.3 Steady state simulation

The aim of the steady state simulation is to directly predict the heat distribution when a system is in radiative equilibrium, without simulating the heat-up process. This simulation was implemented before the heat-up simulation and is very useful for verifying the implemented ray tracing functions. For the analysis of ceria structures, the steady state simulation might be less

appropriate than the heat-up simulation, as during the reduction step the reactor cavity is in a continuous heat-up process and does not even reach steady state [15, 19, 39].
The algorithm for the steady state simulation differs from the one for the heat-up simulation. The steady state simulation is based on the fact that in radiative equilibrium, at each surface point the net radiation is zero. In the simulation environment this means, at each triangle the incoming and outgoing radiation must be equal. The idea for this algorithm was presented in [19] and will be described next.

In the steady state simulation, a ray does not carry an amount of energy, but each ray represents one unit of radiant power:

$$p_{ray} = P_{LS}/n \tag{3.17}$$

where p_{ray} denotes the power that one ray represents, P_{LS} is the total power emitted by the light source and n the total number of rays. For example, assuming a light source with radiant power of 4000 Watts. If the simulation uses 2000 rays, each ray would represent 2 Watts of radiant flux from the ray source to the ray destination.
A fixed amount of rays are started from the light source (only light source, but not from other solid objects) and traced until they hit a solid geometry. The sampling of the starting point and direction is the same as in the heat-up simulation. At the hit point, it is determined whether the ray is absorbed or reflected. If the ray is reflected, just a reflection direction is sampled and the ray tracing continues.
If the ray is absorbed, one major difference in the two algorithms happens at this point: As previously stated, in steady state the incoming radiative flux must be equal to the outgoing radiant flux for each triangle. So if a ray is absorbed, a counter at this triangle is increased by one and the ray is re-emitted. There is no deposition of energy, as only the number of rays absorbed (which is equal to the number of rays re-emitted) at the triangle is of interest. Knowing the number of rays that are re-emitted at a triangle allows to derive the outgoing radiative flux for this triangle:

$$P_i = \sum_r \mathbf{1}_{r,i} * p_{ray} \tag{3.18}$$

where P_i denotes the radiative power of triangle i and p_{ray} is the power that is represented by one ray. $\mathbf{1}_{r,i}$ is an indicator function that is 1 if a ray r is absorbed by triangle i and 0 otherwise. Note that reflections and re-emissions count as separate rays r in 3.18.
In our example, assuming that during the simulation 1000 rays were absorbed and re-emitted at a triangle. It can be derived then that this triangle must radiate with a radiant power of 2000 Watts at steady state. Together with the triangle area and the solid emissivity, the temperature of each triangle can be calculated by the Stefan Boltzmann law 3.1.

$$T_i = (P_i/(A_i\varepsilon_i\sigma))^{\frac{1}{4}} \tag{3.19}$$

where T_i denotes the temperature, P_i the radiative power, A_i the area and ε_i the emissivity of triangle i and σ the Stefan Boltzmann constant.

In the steady state simulation, each ray is traced until it leaves the simulation environment through the aperture. This means a ray is stopped once it hits the light source geometry.
The steady state simulation does not run over several rounds. However, this is only possible as all the material properties are assumed to be temperature independent. In order to use temperature dependent emissivity and heat sinks, a steady state simulation would also have to run over several rounds. In each round these temperature dependent values would be adapted with the temperature estimated in the previous round, until the algorithm converges.

Chapter 4

Implementation

4.1 Software properties

The simulation software is written in C++ and was developed on macOS. It uses CMake to manage the build process and complies with the C++11 standard, therefore cross-platform usability is prepared, even though the software was not yet tested on a different operating system due to time limitations. The development largely followed a test-driven approach, using the unit testing library Google Test [16]. The developed code is therefore divided into two parts, the main application and the testing section. Both are compiled into separate executable files so that the testing section can run as a standalone application.
The ray tracing is based on Intel®, Embree, which is an Open Source collection of high-performance ray tracing methods developed at Intel [37]. Embree is used for the geometrical representation of the 3D objects and enables efficient computation of ray intersections with object surfaces. Additionally, the Open Source geometry processing library libigl [22] is used for operations such as reading, writing and preprocessing of triangulated meshes. Libigl additionally features some visualization tools that were used in the testing section to visually inspect the program behavior.
The software is based on the C++ template library Eigen which is designed for linear algebra [17]. Eigen comes with a variety of functions for matrix and vector calculus and allows data structure access similar to other programming languages. This should make it easier for programmers with

different backgrounds to get familiar with and extend the written code.

4.1.1 Input: Configuration

To launch the application, the user has to provide a configuration file for the simulation. The configuration file uses an INI file format which is well readable for humans and easy to parse. First, the user needs to define whether the steady state or heat-up simulation should be performed. Depending on the simulation type, the two configuration file structures differ, as some parameters are only needed in either the steady state or the heat-up simulation but not in both.
For each object in the simulation environment an STL-file containing the triangulated surface mesh must be provided. The simulation configuration requires some general parameters, such as the number of rays that should be casted in the steady state simulation or the average ray energy in the heat-up simulation.
For each object in the simulation environment, some specific settings are required. In the heat-up simulation for example, for all solid objects some physical properties such as density, specific heat-capacity or initial temperature must be provided.

4.1.2 Output: Simulation results

The output format is similar for both simulations. During the simulation, some information about the simulation progress is printed into the standard output. In both simulations, the simulation results can be written to disk in HDF5 file format. In the heat-up simulation, the simulation results of each round are saved. For each triangle, the amount of emitted and absorbed energy as well as the new temperature is logged. While this slows down computation and can easily lead to large output files, it helped to verify the simulation algorithm, as properties such as energy conservation could be analyzed afterwards. In a further development step, one could include the option to define ”checkpoints” at which the round results should be stored. Additionally, some information such as the round time and the energy lost through the aperture is logged as well for each round.

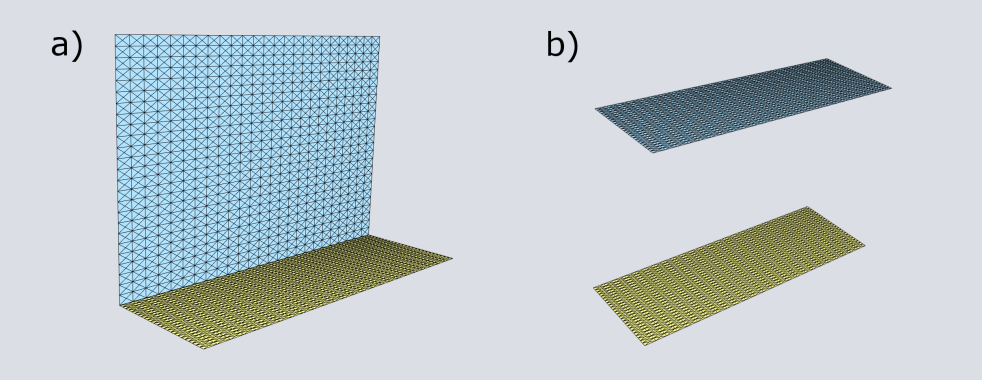

Figure 4.1: Two simple geometrical realations based on rectangles used for configuration factor verification. The source surface is colored yellow (light source), the destination surface is colored light-blue (solid object). (a) Two unequal rectangles connected at an angle of 90°. (b) Two identical, parallel rectangles.

The output for the steady state simulation consists mainly of the absorption counter for each triangle. In both simulations, the area per triangle and the triangle's centroid is logged, so that insights about the heat distribution in 3D space can be inferred without the need of the input STL files.

4.2 Verification

As the testing section was build up together with the main application, the incrementally developed code was tested on a regular basis. This section describes the methods used so far to verify the model and implementation.

4.2.1 Configuration factors

The configuration factor $F_{A\to B}$ denotes the fraction of radiation leaving surface A which arrives at surface B [20]. While generally the computation of configuration factors (also known as view factors) is difficult, for some simple geometries closed-form expressions or tabulated forms exist [20]. Two simple geometrical relations based on rectangles can be seen in Figure 4.1.

The ray tracing can be verified by approximating the configuration factors for such simple geometrical relations. For the scenarios in Figure 4.1 the steady state simulation is used with a full-angle diffuse light source (yellow)

and a perfect absorbing plate (light-blue, reflectivity = 0). We can count how many rays are absorbed at the plate compared to the total number of rays, which is an approximation for the configuration factor $F_{L\to P}$, where L denotes the light source and P the plate. Additionally, by counting how many rays hit the light source from all rays that were re-emitted at the plate, we can get the inverse configuration factor $F_{P\to L}$. Note that in the scenario in Figure 4.1 (b) $F_{L\to P} = F_{P\to L}$ due to symmetry, which is not true for the scenario displayed in in Figure 4.1 (a).

4.2.2 Steady state temperatures

When using a light source which diffusely radiates at the full angle (180°) in a closed, perfectly insulated system, the entire system will reach a temperature equivalent to the black body temperature of the light source. This is a trivial fact as there is no other heat source or sink in the system.
This fact was used to check whether (a) the steady state simulation will reach this temperature at every triangle in the scene and (b) whether the heat up simulation will eventually converge to this state when the simulation time is large enough. For both simulations this could be verified with different cavity geometries, the accuracy depends on the number of rays. In the heat up simulation also initial temperatures that were higher than the black body equivalent temperature of the light source were used and a cool-down to the correct temperature was observed.

4.2.3 Energy balances

Additionally, for the heat up simulation the temperature change based on the emitted and absorbed energy was verified. One way of doing that was to use a closed solid object (cube) and an external light source (at a small distance outside the cube) and ensured that the entire radiation from the light source would hit the cube. The radiation from the light source was fully absorbed by the cube walls and re-radiation from the cube walls was restricted to be to the interior of the cube, therefore no rays could leave the system. In this scenario, it was checked after each round whether the temperature of the cube walls matches with the total energy added to the

system so far.
Similarly, in a regular heat up scenario where the light source is part of the cavity (in the sense of an aperture), the energy balances with the aperture as heat loss at each triangle were analyzed and could it could be verified that no energy is created or lost unintentionally.
As discussed previously, the inhomogeneous energy distribution due to the limited number of rays leads to an "early energy saturation" of the system.

4.3 Performance

4.3.1 Computation time

The performance measurements were performed on a standard MacBook Pro (Late 2013, 2.4 GHz Intel Core i5, 8 GB RAM). To analyze the ray tracing performance, a simulation environment similar to the HFSS cavity was chosen, which was presented earlier in Figure 3.1 (a). The reactor cavity mesh consisted of 25100 triangles, the light source of 100 triangles. The steady state simulation was initialized with 1 million rays that were started from the light source. The cavity boundary was initialized with a reflectivity of 0.5, each ray was traced until it left the cavity through the aperture (when a ray hit the light source geometry). The simulation was repeated 10 times. The total amount of rays that were casted, considering all re-emissions and reflections, was 68.29 million rays with a standard deviation of 0.50 millions. The mean time for this simulation was 45.72 seconds with a standard deviation of 0.78 seconds.
On average, 4.8 rays were lost in the simulation environment, meaning they could escape the closed simulation environment due to numerical issues in the ray-surface-intersection method from Embree. This value is negligible compared to 68 million rays of a simulation run.

Using a profiler, it was observed that most computation time is spent for the calculation for ray-surface-intersections performed by Embree. In the steady state simulation, it consists of around 80% of the total simulation time. The ray sampling process consumed around 12% and post-intersection calculations (counter updates etc.) around 8%. Similarly, in the heat-up

simulation, the intersection calculations were responsible for 70%, the ray sampling process for 11% and the post-intersection calculations for 19% of the total simulation time.

The computation time for the heat-up simulation is determined by the number of rays that are used. The number of rays that are casted in each round depends on the heat distribution and the round time. As discussed earlier, both of these values depend on the meshing, as very small triangles are problematic in the current implementation. Additionally, the minimal ray energy threshold defines the number of re-emissions a ray undergoes. For the same simulation environment as described before, a heat-up simulation with the following settings was initialized: Light radiant power = 4000 K, average ray energy = 10 J, minimal ray energy threshold = 0.1 J, maximal time per round = 10 sec, maximal energy loss per triangle per round = 20%. The solid was initialized with a temperature of 1073 K. The total number of heat-up rounds was set to 1000, the experiment was repeated 10 times. The simulation time was 47.56 seconds with a standard deviation of 4.3 seconds. The total *virtually simulated* time of the heat-up process was around 53 seconds for this 1000 rounds.

4.3.2 Numerical issues

Generally, all computations in the simulation use double precision. Embree uses floating point precision to represent 3D objects, which allows faster intersection computation than double precision would. As discussed previously, floating point precision is still much higher than the precision that can be achieved for physically producing ceria structures. In the ray tracing algorithm, this numerical limitation has a notable impact, however. An intersection point of a ray with a triangle (or the ray starting point sampled from a triangle) can slightly differ from the plane spanned by the three triangle vertices. It therefore happened in the first implementation that the starting point of some rays was slightly behind the triangle from which the ray should start and therefore the ray directly intersected with this triangle (again).
Therefore, a check was added in the intersection routine that disallows the

start and hit triangle to be equal, which solved the problem.

One remaining numerical issue observed so far is the size of the triangle area. Due to the numerical limitation of the vertices precision (floating point), it might happen that two triangle vertices collapse onto the same, rounded position. The triangle area then is zero, and therefore the associated mass and heat capacity of the triangle is zero as well. Not only vanishing but also very small triangles are problematic.
Firstly, only one ray hitting this very small triangle and depositing some energy might be enough to unnaturally boost the temperature of this triangle. Secondly, the small heat capacity limits the possible round time, as only a maximal temperature drop per triangle per round is allowed. Triangles with zero area are neglected in the current implementation, however otherwise the user is responsible for providing inputs with appropriate meshes.

4.4 Further improvements

Some options for further development were already mentioned during this report, which have not yet been implemented due to the limited amount of time. This include for example a better volume representation in the model, temperature dependent physical properties of the materials and cross-platform support.
One goal that could not be achieved so far is the parallelization of the ray tracing. As all the rays in one round can be treated as individual events, there is a lot of potential for increasing the performance. The calculation for finding the intersections, performed by Embree, is parallelized, the remaining parts of one ray tracing round happens sequentially so far.

Chapter 5

Design guidelines for ceria structures

5.1 Insights from related work

Beside the ordered structures presented in Figure 2.3, [19] analysed different RPC structures that can be seen in Figure 5.1. For all structures a better temperature gradient could be observed compared to a reference RPC element, as less radiation was blocked at the front. The "Frame" structure yielded a better oxygen release per gram ceria than the "Reference" structure. However, the "Reference" RPC block had the highest mass which led to the best performance overall, regarding oxygen release. The concave interior shape of the "Frame" layout leads to a beneficial *cavity effect*. This positive effect could also be observed in the ordered structure layout that is shown in 2.3 and should be considered in the design of new structures [19].
As the production of ordered ceria structures for volumetric heat absorbers is a rather young field of research, extensive studies are missing yet. However, there is interesting related work with other materials than ceria, which will be covered next.

5.1.1 Honeycombs

A honeycomb layout consists of a lot of small, equal sized channels that go through the entire receiver from the front to the back. Generally, honeycomb structures have the same problem as RPC structures: the porosity is constant over the depth and therefore a lot of radiation is attenuated in the front. [28]

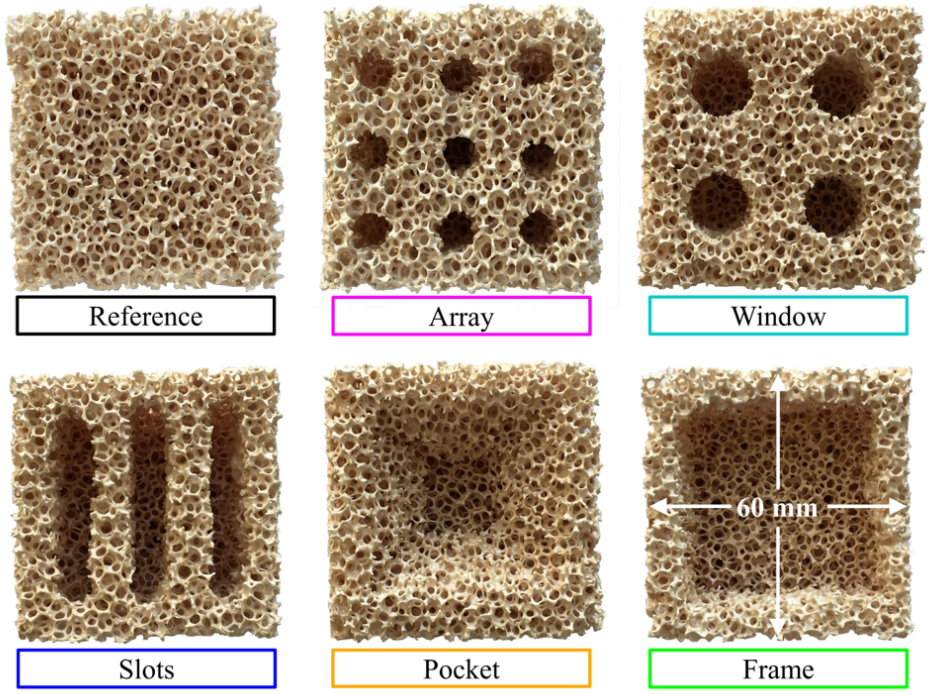

Figure 5.1: Six modified RPC structures. This figure is copied from [19].

analyzed a solar radiation receiver made of an iron based alloy that can be seen in Figure 5.2 (a).

A parameter study was performed for a round receiver with 40mm depth and a layout similar to a honeycomb structure. Various wall thicknesses and channel diameters were tested. It was found that the efficiency is increasing with decreasing wall thickness. An optimum was found for a channel diameter of 0.5 mm and a wall thickness of 0.05 mm. While this cannot be produced with current ceria manufacturing procedures, it would most likely not meet stability requirements as well. However, the ratio of 1:10 for material (wall size) to empty space is interesting and could guide the design for similar structures made of ceria.

5.1.2 Multi-layer designs

[24] presented a multi-layer design for a solar receiver made of stainless steel, featuring volumetric absorption, which can be seen in Figure 5.2 (c).

(a) Honeycomb structure made of an iron based alloy. This figure is copied from [28].

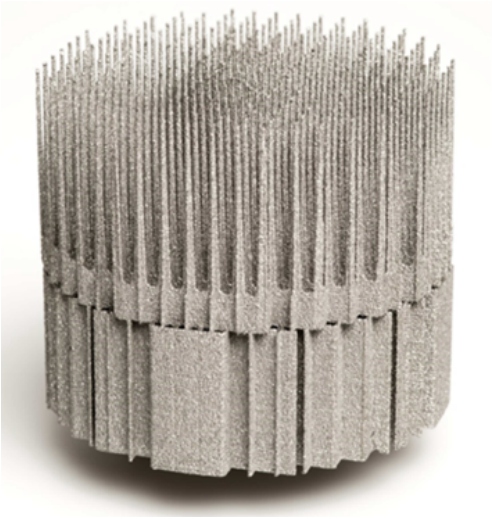

(b) ”Spike” based design for volumetric solar receivers made of metals. This figure is copied from [5].

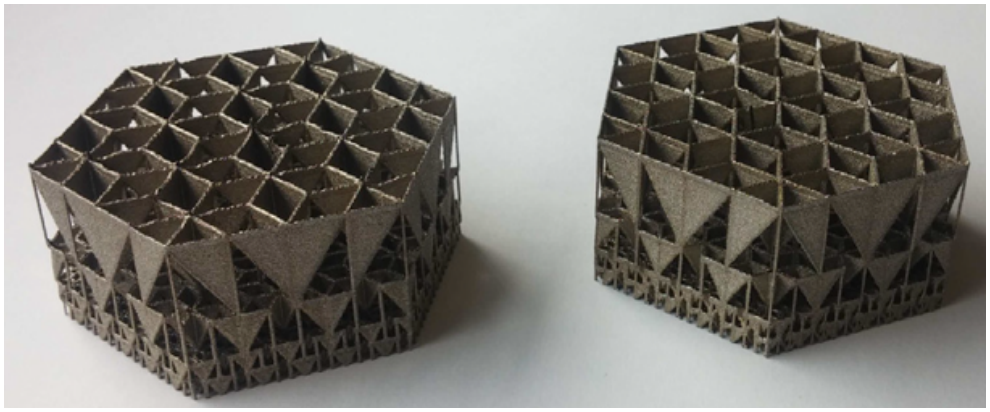

(c) Multi-layer structure with decreasing porosity from top to bottom layers. This figure is copied from [24].

Figure 5.2: Illustrations of volumetric solar receiver designs from related work.

The idea of having multiple layers with different porosities is similar to the one that we have discussed previously with the ordered structures made of ceria by [19]. As discussed earlier, the front struts in the ordered ceria structure blocked too much radiation, while the mass was mainly located at the rear part. It could be that the volume directly behind the front struts could have been filled with ceria material, as this part was mostly in the "shadow" region of the front struts anyway and would not have contributed to direct re-radiation too much. This seems to be the idea behind the design showed in 5.2 (c), which uses triangle-shaped side walls (parallel to the incident radiation direction) for the base geometry, instead of only struts. In both multi-layer designs (2.3 and 5.2 (c)) it was observed, that the most radiation attenuation happens at the layer boundaries. This seems intuitive, as the surface area there is orthogonal to radiation direction.

5.1.3 Spikes

[5] analyzed the common honeycomb structures for volumetric solar receivers made of ceramics or metals and presented a "spike" based design that can be seen in Figure 5.2 (b). It is basically a honeycomb structure, where the side walls of the channels have been eliminated to a vast amount. The remaining structure consists of many thin spikes, which reminds of a nail board. This design showed a performance increase of around 12% compared to a conventional honeycomb absorber. Such a design is most likely hard to achieve with ceria, as thin spikes might be too fragile. However, the idea behind this structure seems promising, as there are no layer boundaries at which a lot of incoming radiation would be stopped.

5.2 Design goals

As previously discussed, an optimal ceria structure for a given volume features a high mass, high specific surface area and a shape that allows a large fraction of incoming radiation to penetrate till the rear part. The analysis of related work confirmed the intuition that the major sources of undesired re-radiation are surface parts which are orthogonal to the incoming radiation.

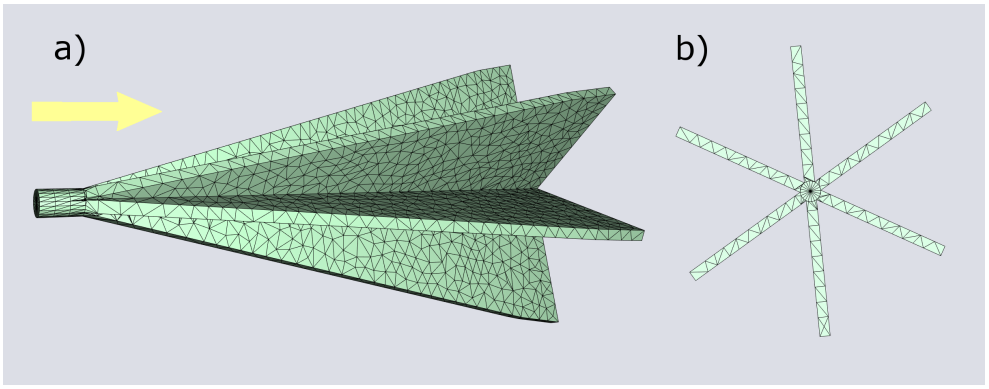

Figure 5.3: Basic tree element. (a) 3-D illustration. The yellow arrow denotes the main direction of radiation. (b) Top-view of the basic tree element.

Such areas should therefore be minimized in a shape design. Additionally, a structure which can somehow "trap" incoming radiation would lead to a desired cavity effect.

A concrete design suggestion that follows these guidelines is presented now. Instead of using a multi-layer setup with *constant* porosity at each layer, the novel design idea for a structure features a *continuously* decreasing porosity from the front to the back. The structure is built up from basic elements which will be called *trees* in the following. Such a basic tree element can be seen in Figure 5.3 (a). The yellow arrow denotes the main direction of radiation, which is from the cavity center to the cavity boundary.
Multiple trees would then be arranged in the solar reactor, so that the tree tips point towards the center of the reactor. A possible arrangement of trees in a solar reactor cavity can be seen in Figure 5.4. The pattern to align neighboring trees could for example be just simple squares or a hexagonal layout. However, it is important to gain insights about the optimal shape of a single tree first, the study of arrangements of multiple trees in the reactor will be a second step.

Each tree consists of a set of *lamellas* which are allocated circularly around the tree center. Each lamella has a fixed thickness (e.g 1 mm), width (e.g. 15 mm) and height (e.g. 50 mm). The lamella width defines the radius of the tree at the bottom, the lamella height defines the height of the tree. An illustration of a single lamella can be seen in Figure 5.5 (b).

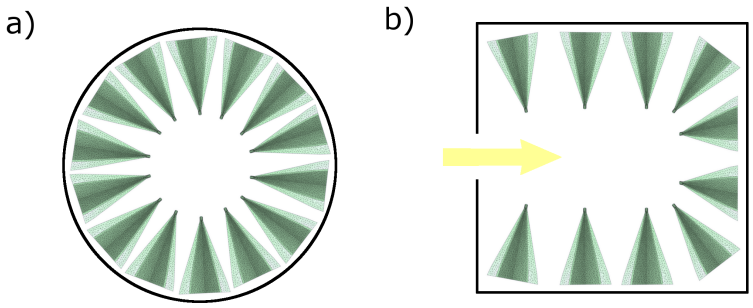

Figure 5.4: Illustration of a possible tree arrangement layout in a cylindric reactor cavity. (a) Front-view (or vertical cross-section) of the cavity. (b) Top-view (or horizontal cross-section) of the cavity. The yellow arrow denotes the incoming light through the aperture.

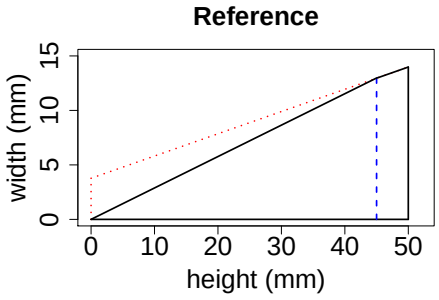

(a) Width versus height for the ”Reference” shape.

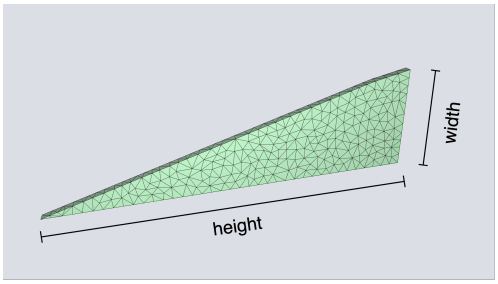

(b) 3-D illustration of a single lamella with ”Reference” shape. The lamella height and width define the tree size.

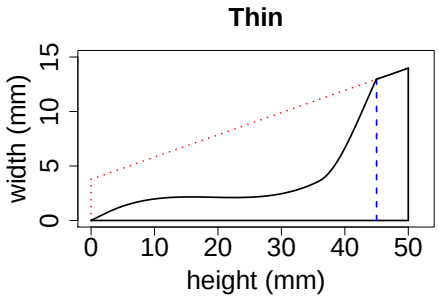

(c) Width versus height for the ”Thin” shape.

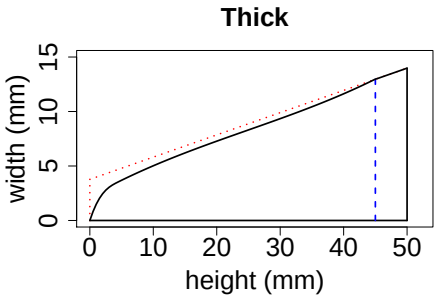

(d) Width versus height for the ”Thick” shape.

Figure 5.5: Illustrations of the three lamella shapes ”Reference”, ”Thin” and ”Thick”. In (a), (c), and (d), the red dotted lines indicate form constraints, the blue dashed line indicates the start of the offset-area.

By using a tree as described above as a basic element, the following beneficial design feature is expected: With varying the number and shape of the lamellas, one can gradually control the mass distribution and average ray penetration depth. The tree in Figure 5.3 (a) is built up from 6 equal lamellas with height 50 mm and would fit into a hexagon with inner radius of 15 mm at the bottom.
Three possible lamella shapes are illustrated in Figure 5.5. The ”Reference” lamella shape in Figure 5.5 (a) is a simple triangle. For the ”Thin” and ”Thick” lamella shapes the outer edge (hypotenuse) of the triangle was altered to a smooth curve (Figures 5.5 (c) and 5.5 (d)). This shrinks or enlarges the volume of the lamella.
Each lamella has an offset part at the bottom, which is indicated by the blue dashed line. An offset part is needed so that neighboring trees are physically connected at the bottom. For these shape designs it was assumed that the reactor cavity would have the form of a sphere instead of the actual cylinder. This is a simplification for a tree arrangement like in Figure 5.4 (b), where all trees would point towards the reactor center. This assumption induces some form constraints that are indicated by the red lines. It is assumed that the sphere has a radius of 75 mm (radius of the HFSS at ETH Zurich [11]). Each each tree would therefore have to fit into a hexagonal cone (with tip at the center of the sphere) of height 75 mm and inner radius of 15 mm. With a tree height of 50 mm and an empty space between the tree bottom and the reactor cavity of 5mm, an empty area with radius of 20 mm would be in the center of the sphere. For an acutal tree arrangement these values would change, however it serves as a uniform setup for analyzing different tree shapes.

5.3 Experimental

The heat-up behavior of three different tree structures was analyzed using the heat-up simulation developed in this thesis. The corresponding lamella shape designs for the ”Reference”, ”Thin” and ”Thick” tree structure were introduced in the previous chapter in figure 5.5. The number of lamellas per tree was set to 12 for the experiments.

5.3.1 Experimental setup

The triangulated surface mesh for each structure was generated using the geometry processing library libigl ([22]) in C++. As the surfaces showed some undesired artifacts and triangle sizes that strongly varied, the objects were re-meshed using the software Meshmixer [3]. In each simulation, not a full tree but only one-third (120°) of a tree was used in combination with mirror planes (fully specular reflective walls) due to rotational symmetry for saving computation time. A simulation segment had therefore the shape of a third of a hexagonal cone and each tree segment consisted of 4 lamellas. The three simulation environments can be seen in Figure 5.6. The outer walls of the hexagonal cone were implemented with mirror planes as well for simulating the spherical form of the tree arrangement. All four mirror planes are transparent in each illustration of Figure 5.6. Note that this mirroring is not perfect, as a sphere cannot be made of unique sized hexagons. However, this was assumed to be a better approximation than for example an infinite cylinder that could be simulated with approximately similar effort with mirrors.
Furthermore, a reactor cavity with 75 mm radius and a tree of height 50 mm with 15 mm radius at the bottom were assumed. Under these constraints, a hexagonal cone has an angle of 23.07°. Using a tree layout as in Figure 5.4 (b) one could fit approximately 48 trees into a cavity similar to the HFSS (space for cerium laminate is ignored here).

Light source
A light source with 4 kW power was assumed for the full reactor. The power for the light source in the segment was adjusted so that the ratio of power to area was equal for the full reactor and the simulation segment light source. In this configuration, the steady-state temperature in the simulation segment equals the steady-state temperature in the full reactor under the assumption of perfect insulation and diffuse radiation from both light sources. Note that the concentrated solar irradiation is actually not equally distributed in the reactor cavity. However, at some point in the heat-up process, the re-radiation from other ceria segments dominates the irradiation from the aperture for one segment.

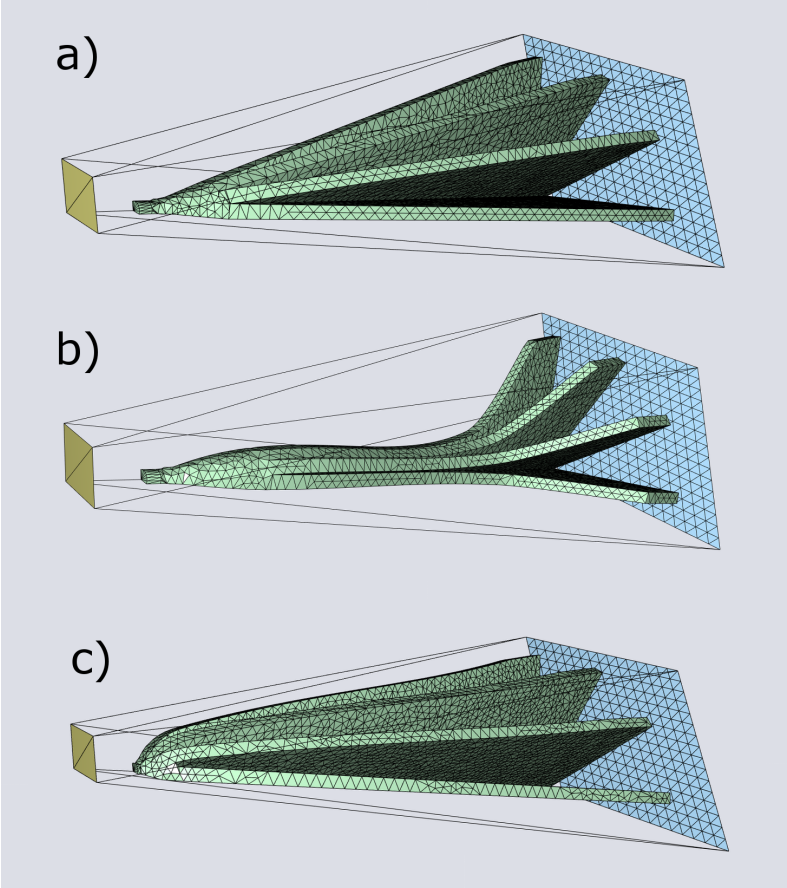

Figure 5.6: 3-D illustrations of the three simulation segments. (a) ”Reference” tree segment. (b) ”Thin” tree segment. (c) ”Thick” tree segment. The yellow area deontes the light source, the light-blue area denotes the cavity boundary. Transparent planes are mirrors.

The chosen setup can be thought of as a spherical light source (with 4 kW power) in the center of a spherical reactor. The area of the segment light source was chosen to be $\frac{1}{3*48}$ of the aperture size of the full reactor (48 trees, one-third of a tree is simulated). The size of the light source area in the segment defines the amount of re-radiation loss and has therefore an influence on the heat-up time.

Cavity boundary

For the cavity boundary (which is colored light-blue in the illustrations of Figure 5.6), an Al_2O_3-SiO_2 material with the following parameters were assumed: thickness = 20 mm, reflectivity = 0.72, density = 560.65 kg/m^3, spe-

Structure	# Triangles	Total mass [g]	Avg. mass per triangle [mg]
Reference	6931	6.557835	0.94616
Thin	4480	3.332916	0.7439544
Thick	11722	7.624902	0.6504779

Table 5.1: Number of triangles, total mass and average mass per triangle for the three analyzed structures.

cific heat capacity = 1109 J/(kg * K). The values for reflectivity and density are obtained from [15] directly, the values for specific heat capacity are in the range of 1096 - 1118 J/(kg * K) for a temperature range of 1100 - 1800 K, an average value for the temperature of 1500 K was chosen [15].

Ceria structure

For the ceria material (which is colored green in the illustrations of Figure 5.6) the following parameters were chosen: thickness = 0.5 mm, reflectivity = 0.24, density = 5415 kg/m^3, specific heat capacity = 418 J/(kg * K). The value for reflectivity is obtained from [15] directly. The value for the density is calculated assuming a microporosity of 25% ([31]) and a ceria density of 7220 kg/m^3 [15]. The value for the specific heat capacity is computed for a temperature of 1500 K analogue to that of the cavity boundary.

5.3.2 Mass distribution

The number of triangles after re-meshing, total mass of the structure and average mass per triangle can be see in table 5.1. Note that the total mass represents one-third of a tree.

The distribution of the masses within the structures can be seen in Figure 5.7. A binning with bin size of 0.5 mm in the direction of the height of the tree was used. The mass distributions are as expected, when compared with the design of the tree shapes from Figure 5.5. It can be seen that the mass at the bottom of the tree (at height = 50 mm) does not follow the trend of the previous bins and is much higher. This is due to the simplified volume representation, as the volume area at the very bottom is counted twice. At the sharp edge at the bottom, the volumes associated to triangles from the

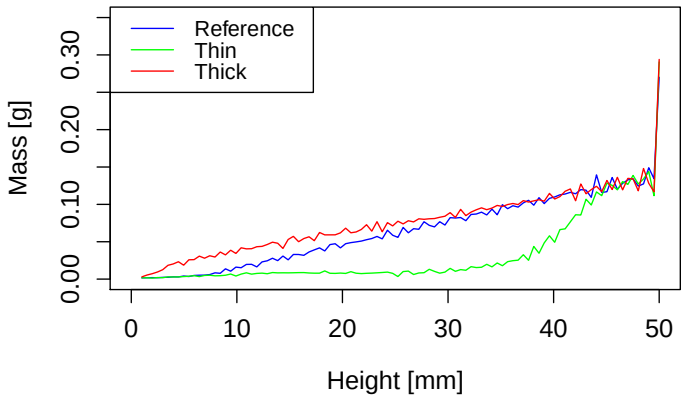

Figure 5.7: Mass versus height for the three analyzed structures. Values were calculated from a binning in direction of height with 0.5 mm bin-size.

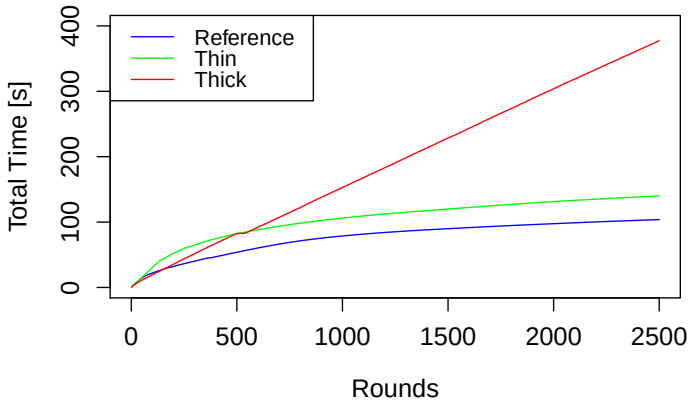

Figure 5.8: Total elapsed time versus round numbers for the three simulation runs.

side and bottom walls of each lamella overlap.

5.3.3 Temperature analysis

Figure 5.8 shows the total time evolvement for the three simulation runs. The simulation for the ”Thick” tree structure shows a much larger average

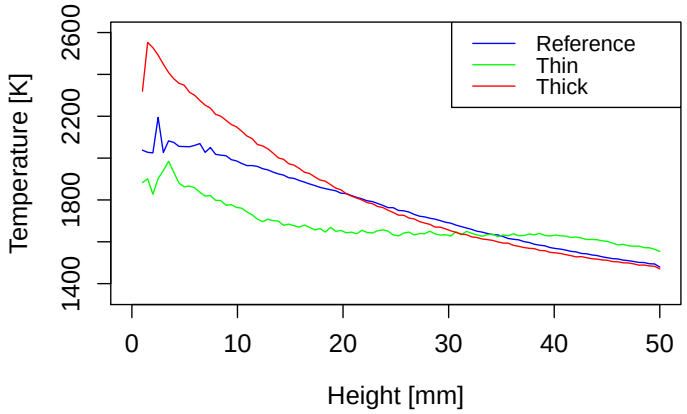

Figure 5.9: Temperature versus height for the three analyzed structures at the checkpoint when half of the mass exceeds 1500 K. Values were calculated from a binning in direction of height with 0.5 mm bin-size.

round time. It is expected that after the re-meshing, the "Thick" structure had generally a more uniform triangulation than the other structures, leading to less small triangles which may dump the round time. This effect was underestimated in the re-meshing process.

For illustrating the temperature analysis, a specific checkpoint was defined as "the point in time when half of the mass of a structure exceeds 1500 K". For the "Reference" structure, this was after 89.5 seconds, for the "Thin" structure after 57.1 seconds and for the "Thick" structure after 176.8 seconds of virtual simulated time. The temperature distributions at this checkpoint for each structure are compared in Figure 5.9. It can be seen that the "Thick" structure has the largest temperature gradient at this checkpoint, followed by the "Reference". The "Thin" structure shows the lowest temperature gradient which matches with the expectations. It must be noted that all three simulations will eventually converge to a steady state temperature of around 2727 K, due to the chosen light source representation. This is much higher than maximal temperatures usually observed in real experiments, which are around 2250 K [15]. In these experiments, a ceria structure thickness of 0.5 mm was chosen based on the lamella thickness of 1 mm. For the tip of the

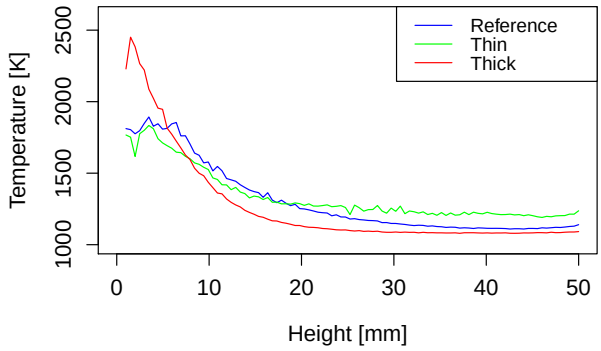

(a) Temperature distributions after 10 seconds.

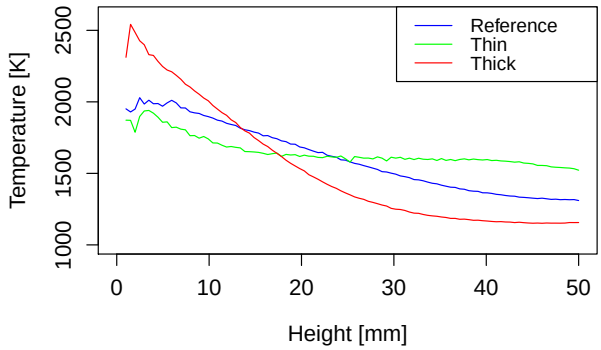

(b) Temperature distributions after 50 seconds

Figure 5.10: Temperature versus height for the three analyzed structures at a specific point in time. Values were calculated from a binning in direction of height with 0.5 mm bin-size.

structures, this results in triangles with low mass which are directly exposed to high radiative flux, which might explain the extremely fast heating and hot temperatures predicted at these locations (above sublimation temperature of ceria).

Similar temperature distributions can be found when comparing the heat-up processes at a given time for all structures. Figure 5.10 shows the temperature differences observed in the three structures after 10 and 50 seconds.

Using the mass and temperature predictions for all triangles, one can then find the specific oxygen release for a structure [4]. This could then be used as a metric for evaluating the performance of a certain structure. Additionally, one could analyse the energy balances such as the energy loss at the aperture, similar to how it is shown in Figure A.2 that illustrates the energy saturation problem.

Chapter 6

Conclusion and Outlook

During this thesis, a virtual simulation environment for the analysis of the heating behavior of ceria structures in solar reactor cavities was developed. The potential of the simulation was demonstrated by experimental simulation runs with ordered structures following a novel design scheme. While some aspects of the simulation algorithm could be verified, a validation process with actual measurements from real experiments in solar reactors is needed. This could be achieved by using 3-D models from structure layouts which were already analyzed experimentally in a solar reactor.

The design suggestion presented in this thesis is based on guidelines derived from related work and consists of basic elements called *trees*, which are made of a set of *lamellas*. To find an optimal structure based on this design scheme, design parameter studies are needed. For an optimized shape of a single tree one could vary the number and shapes of lamellas. The lamella thickness was set to a constant value in the experiments. This could be changed, so that the lamella is thinner on the top and thicker on the bottom of the tree, for example. Another interesting approach would be to combine different lamella shapes for one tree. Furthermore, the actual tree arrangement in the reactor cavity must be optimized. It might be interesting to use some optimization techniques from the field of topology optimization. A randomized algorithm to find an optimized tree structure, could look as follows:
A set L of n different lamella shapes is generated. A tree is defined to consist

of m lamellas, which would be initialized randomly with lamellas from L. The optimization procedure would run over several rounds. In each round, one lamella of the tree would be replaced by a different lamella from L that leads to a better performance for the tree (using a metric such as oxygen release after a specific heat-up time). The lamella to replace would be chosen randomly, the new lamella candidates would be a subset of L. Convergence is achieved when no performance improvement happens over some rounds. Such a randomized algorithm could be beneficial, as testing all different combinations for m lamellas with n possible shapes would be expensive to compute. Furthermore, many combinations would be very similar for symmetry reasons in the tree, but finding only relevant combinations might be hard to compute, however. For such an algorithm to work, the performance metric must be computed multiple times in each round. As the heat-up procedure runs itself over several rounds, this would result in large computation time. Therefore some optimizations concerning computation time (such as parallelization) are of specific interest.

Generally, it will be beneficial to run virtual simulations with novel structure designs before the physical manufacturing. This can lead to a significant performance increase of solar reactors in the near future and help to establish solar fuels as energy carriers.

Appendix A

Appendix

A.1 Energy saturation problem

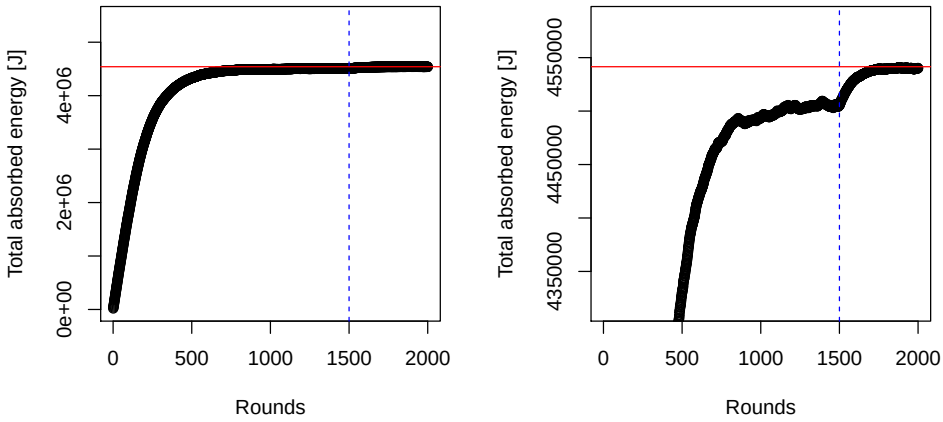

(a) Total energy that was absorbed in the system versus round numbers. Red: Target energy.

(b) Total energy that was absorbed in the system versus round numbers (zoom-in). Red: Target energy.

Figure A.1: Plots for illustrating the total energy absorbed in the system, showing the energy saturation problem. Exemplary environment was an empty cavity in the shape of the HFSS. After 1500 rounds (blue dashed line), the average energy per ray was decreased.

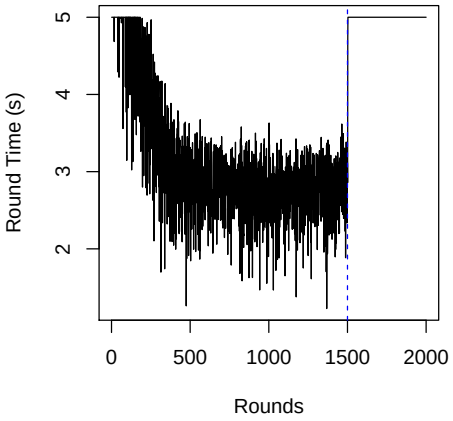

(a) Round time versus round number. A maximal round time of 5 seconds was chosen.

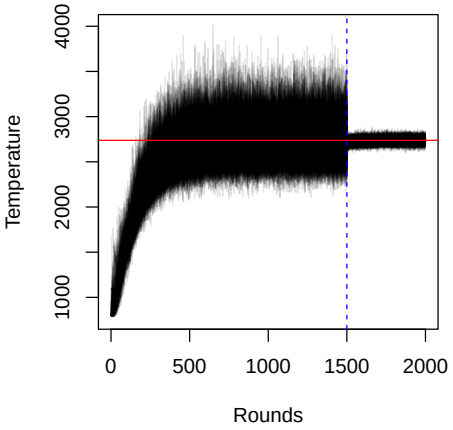

(b) Development of temperature (1% of all triangles used for this illustration). Red: Target temperature.

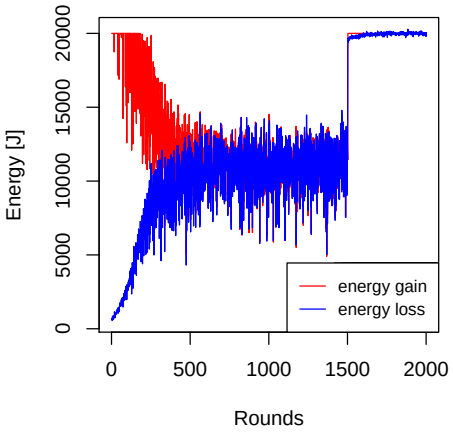

(c) Red: Energy that was added to the system by the light source. Blue: Energy that left the system through the aperture (light source).

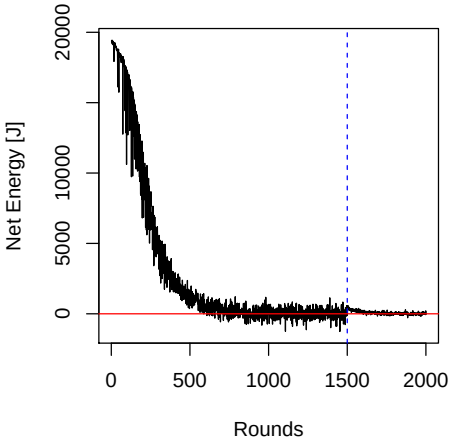

(d) Net energy flow at the aperture (light source). Red: Target net energy flow for steady state.

Figure A.2: Plots of the the heat-up simulation for illustrating the energy saturation problem. Exemplary environment was an empty cavity in the shape of the HFSS. After 1500 rounds (blue dashed line), the average energy per ray was decreased.

Bibliography

[1] S. Ackermann, M. Takacs, J. Scheffe, and A. Steinfeld. Reticulated porous ceria undergoing thermochemical reduction with high-flux irradiation. *International Journal of Heat and Mass Transfer*, 107:439–449, 2017.

[2] D. Arvizu, P. Balaya, L. Cabeza, T. Hollands, A. Jäger-Waldau, M. Kondo, C. Konseibo, V. Meleshko, W. Stein, Y. Tamaura, H. Xu, and R. Zilles. *Direct Solar Energy. In IPCC Special Report on Renewable Energy Sources and Climate Change Mitigation*. Cambridge University Press, Cambridge, United Kingdom and New York, NY, USA., 2011.

[3] Autodesk, San Rafael, USA. Meshmixer, V3.5. www.meshmixer.com, 2020.

[4] B. Bulfin, L. Hoffmann, L. de Oliveira, N. Knoblauch, F. Call, M. Roeb, C. Sattler, and M. Schmücker. Statistical thermodynamics of non-stoichiometric ceria and ceria zirconia solid solutions. *Phys. Chem. Chem. Phys.*, 18:23147–23154, 2016.

[5] R. Capuano, T. Fend, H. Stadler, B. Hoffschmidt, and R. Pitz-Paal. Optimized volumetric solar receiver: Thermal performance prediction and experimental validation. *Renewable Energy*, 114, 2017.

[6] J. Cardoso, F. Mendes, and J. Mendes. HeatTracer - a novel Monte Carlo radiative heat transfer tool for cavity receivers simulation. *AIP Conference Proceedings*, 2126:170003, 2019.

[7] W. C. Chueh, C. Falter, M. Abbott, D. Scipio, P. Furler, S. M. Haile, and A. Steinfeld. High-flux solar-driven thermochemical dissociation of CO2 and H2O using nonstoichiometric ceria. *Science*, 330(6012):1797–1801, 2010.

[8] COMSOL AB, Stockholm, Sweden. COMSOL Multiphysics®. www.comsol.com, 2020.

[9] T. Dbouk. A review about the engineering design of optimal heat transfer systems using topology optimization. *Applied Thermal Engineering*, 112:841–854, 2016.

[10] R. J. Detz, J. N. H. Reek, and B. C. C. van der Zwaan. The future of solar fuels: when could they become competitive? *Energy Environ. Sci.*, 11:1653–1669, 2018.

[11] F. Dähler. Personal communication, ETH Zurich, Zurich, 2020.

[12] O. Edenhofer, R. Pichs-Madruga, Y. Sokona, K. Seyboth, P. Matschoss, S. Kadner, T. Zwickel, P. Eickemeier, G. Hansen, S. Schlömer, and C. von Stechow. *Summary for Policymakers. In: IPCC Special Report on Renewable Energy Sources and Climate Change Mitigation*. Cambridge University Press, Cambridge, United Kingdom and New York, NY, USA., 2011.

[13] T. Fend, R. Pitz-Paal, B. Hoffschmidt, and O. Reutter. Solar radiation conversion. In *Cellular Ceramics*, chapter 5.7, pages 523–546. John Wiley & Sons, Ltd, 2006.

[14] P. Furler, J. Scheffe, D. Marxer, M. Gorbar, A. Bonk, U. Vogt, and A. Steinfeld. Thermochemical CO2 splitting via redox cycling of ceria reticulated foam structures with dual-scale porosities. *Physical chemistry chemical physics : PCCP*, 16:10503–10511, 2014.

[15] P. Furler and A. Steinfeld. Heat transfer and fluid flow analysis of a 4kW solar thermochemical reactor for ceria redox cycling. *Chemical Engineering Science*, 137:373–383, 2015.

[16] Google LLC. Googletest, Google Testing and Mocking Framework. https://github.com/google/googletest, 2020.

[17] G. Guennebaud, B. Jacob, et al. Eigen v3. http://eigen.tuxfamily.org, 2020.

[18] I. Hadjipaschalis, A. Poullikkas, and V. Efthymiou. Overview of current and future energy storage technologies for electric power applications. *Renewable and Sustainable Energy Reviews*, 13:1513–1522, 2009.

[19] M. Hoes. *Redox materials and structures for thermochemical H2O and CO2 splitting cycles*. PhD thesis, ETH Zurich, Zurich, 2019.

[20] J. Howell, R. Siegel, and M. P. Mengüç. *Thermal Radiation Heat Transfer, 5th edition*. CRC Press, 2010.

[21] J. R. Howell. The Monte Carlo Method in Radiative Heat Transfer. *Journal of Heat Transfer*, 120(3):547–560, 1998.

[22] A. Jacobson, D. Panozzo, et al. libigl: A simple C++ geometry processing library. https://libigl.github.io/, 2020.

[23] D. Keene, J. Davidson, and W. Lipiński. A model of transient heat and mass transfer in a heterogeneous medium of cerium dioxide undergoing nonstoichiometric reduction. *Journal of Heat Transfer*, 135:52701, 2012.

[24] S. Luque, G. Menéndez, M. Roccabruna, J. González-Aguilar, L. Crema, and M. Romero. Exploiting volumetric effects in novel additively manufactured open solar receivers. *Solar Energy*, 174:342–351, 2018.

[25] M. C. E. Manuel and P. T. Lin. Heat exchanger design with topology optimization. In *Heat Exchangers - Design, Experiment and Simulation*. S M Sohel Murshed and Manuel Matos Lopes, IntechOpen, 2017.

[26] D. Marxer, P. Furler, M. Takacs, and A. Steinfeld. Solar thermochemical splitting of CO2 into separate streams of CO and O2 with high selectivity, stability, conversion, and efficiency. *Energy Environ. Sci.*, 10:1142–1149, 2017.

[27] C. Minas, D. Carnelli, E. Tervoort, and A. R. Studart. 3d printing of emulsions and foams into hierarchical porous ceramics. *Advanced Materials*, 28(45):9993–9999, 2016.

[28] C. Pabst, G. Feckler, S. Schmitz, O. Smirnova, R. Capuano, P. Hirth, and T. Fend. Experimental performance of an advanced metal volumetric air receiver for solar towers. *Renewable Energy*, 106, 2017.

[29] R. Pullar, R. Novais, A. Caetano, M. Barreiros, S. Abanades, and F. Oliveira. A review of solar thermochemical co2 splitting using ceria-based ceramics with designed morphologies and microstructures. *Frontiers in Chemistry*, 7:601, 2019.

[30] M. Romero and A. Steinfeld. Concentrating solar thermal power and thermochemical fuels. *Energy Environ. Sci.*, 5:9234–9245, 2012.

[31] P. Roos. Design, fabrication, and testing of large scale ceria rpc structures for a cavity-based 50 kw solar reactor. Master thesis. ETH Zurich, Zurich, 2016.

[32] J. Scheffe and A. Steinfeld. Oxygen exchange materials for solar thermochemical splitting of H2O and CO2: A review. *Materials Today*, 17:341–348, 2014.

[33] K. Schwartzwalder, H. Somers, and A. Somers. US Patent 3,090,094. https://patents.google.com/patent/US3090094A, 1963.

[34] S. Silvestri and R. Pecnik. A fast GPU Monte Carlo radiative heat transfer implementation for coupling with direct numerical simulation. *Journal of Computational Physics: X*, 3:100032, 2019.

[35] A. Steinfeld. Solar thermochemical production of hydrogen - a review. *Solar Energy*, 78:603–615, 2005.

[36] V. Subramaniam, T. Dbouk, and J.-L. Harion. Topology optimization of conjugate heat transfer systems: A competition between heat transfer enhancement and pressure drop reduction. *International Journal of Heat and Fluid Flow*, 75:165–184, 2019.

[37] I. Wald, S. Woop, C. Benthin, G. S. Johnson, and M. Ernst. Embree: A kernel framework for efficient cpu ray tracing. *ACM Trans. Graph.*, 33(4):143, 2014.

[38] H. G. Weller, G. Tabor, H. Jasak, and C. Fureby. A tensorial approach to computational continuum mechanics using object-oriented techniques. *Comput. Phys.*, 12(6):620–631, 1998.

[39] S. Zoller, E. Koepf, P. Roos, and A. Steinfeld. Heat transfer model of a 50 kW solar receiver–reactor for thermochemical redox cycling using cerium dioxide. *Journal of Solar Energy Engineering*, 141(2):021014, 2019.

Eidgenössische Technische Hochschule Zürich
Swiss Federal Institute of Technology Zurich

Declaration of originality

The signed declaration of originality is a component of every semester paper, Bachelor's thesis, Master's thesis and any other degree paper undertaken during the course of studies, including the respective electronic versions.

Lecturers may also require a declaration of originality for other written papers compiled for their courses.

I hereby confirm that I am the sole author of the written work here enclosed and that I have compiled it in my own words. Parts excepted are corrections of form and content by the supervisor.

Title of work (in block letters):

Modeling of heat transfer in structured ceramic materials

Authored by (in block letters):

For papers written by groups the names of all authors are required.

Name(s):	**First name(s):**
Müller	Fabian

With my signature I confirm that

- I have committed none of the forms of plagiarism described in the 'Citation etiquette' information sheet.
- I have documented all methods, data and processes truthfully.
- I have not manipulated any data.
- I have mentioned all persons who were significant facilitators of the work.

I am aware that the work may be screened electronically for plagiarism.

Place, date	**Signature(s)**
Zurich, 21.04.2020	

For papers written by groups the names of all authors are required. Their signatures collectively guarantee the entire content of the written paper.